IEEE Access
Multidisciplinary | Rapid Review | Open Access Journal

Received June 17, 2020, accepted June 29, 2020, date of publication July 10, 2020, date of current version July 24, 2020.

*Digital Object Identifier 10.1109/ACCESS.2020.3008429*

# A Wide Incident Angle, Ultrathin, Polarization-Insensitive Metamaterial Absorber for Optical Wavelength Applications

**SULTAN MAHMUD[1,2], SIKDER SUNBEAM ISLAM[1], (Member, IEEE), ALI F. ALMUTAIRI[3], (Senior Member, IEEE), AND MOHAMMAD TARIQUL ISLAM[2], (Senior Member, IEEE)**

[1]Department of Electrical and Electronic Engineering, International Islamic University Chittagong, Chittagong 4318, Bangladesh
[2]Department of Electrical, Electronic and Systems Engineering, Faculty of Engineering and Built Environment, Universiti Kebangsaan Malaysia, Bangi 43600, Malaysia
[3]Electrical Engineering Department, Kuwait University, Kuwait City 13060, Kuwait

Corresponding authors: Sultan Mahmud (sultaniiuc3ni@gmail.com), Ali F. Almutairi (ali.almut@ku.edu.kw), and Mohammad Tariqul Islam (tariqul@ukm.edu.my)

**ABSTRACT** Polarization-insensitive metamaterial absorbers (MMAs) are currently attracting a great deal of interest throughout the optical region. These kinds of MMAs can be used as energy harvesting, thermal imaging, plasmonic sensor, magnetic imaging, light trapping, optical modulator, and can help to decipher an inherence for the field. Here, a polarization-insensitive ultrathin MMA has been proposed with an extensive incident angular stability for the optical region with a sandwiched three-layer structure. Tungsten (W) and silicon dioxide ($SiO_2$) have been chosen as materials for their various advantages in the optical spectrum with higher temperature stability. The design simulated with the finite integration technique (FIT), and validation of the simulated data is assured with the interference theory model (ITM). Underlying physics of the absorption characteristics and performance of the structure are immensely explained. The design acquired an average absorption of 96.7% from 380nm to 700nm and 96.61% for both transverse electric (TE) and transverse magnetic (TM) polarization. It has a peak absorption of 99.99% at 498.25nm, and over 99% from 460nm to 540nm, due to a very good impedance match with plasmonic resonance characteristics. For both TE and TM mode, it has wide angular independence up to 60°, which can be used for solar cell and solar thermo-photovoltaics (STPV). The various parametric sweep also analyzed for acquiring the geometric shape with a wide bandwidth to find resonance wavelength. As the MMA shifts its resonance wavelength with the change of its dielectric thickness, it can be used as an optical sensor. Changing dielectric in a Pyrex will enable the structure to be used as a light detector. Such outstanding absorption properties render the proposed MMA a successful candidate for the optical wavelength applications mentioned above.

**INDEX TERMS** Polarization-insensitive, metamaterial absorber, incident angular stability, impedance match, plasmonic resonance characteristics.

## I. INTRODUCTION

Theoretical explanation of V. Veselago devotee Smith *et al.* to find an artificial double negative (DNG) metamaterial with negative permeability and permittivity [1], [2]. These proper-ties of metamaterials depends on their physical structure that enables them to be used as antennas [3], waveguides [4], filters [5], invisible cloaks [6], absorbers [7], [8], specific absorption rates (SAR) [9], [10], detectors [11], imaging[12], RF lenses [13], superlenses [14], polarization converter [15], various kind of sensors [16]–[19]. After the first corroboration of metamaterial absorbers (MMA) in 2008 by Landy *et al.*, they have been studied vigorously, both theoretically and practically [20]. In the same year, Tao *et al.* demonstrated a single and THz MMA at 1.3 THz, which opened the door for THz applications [21]. THz metamaterials can be differentiated by single band [22], dual-band [23], [24], multi-band [25], [26], tunable [27], [28],

The associate editor coordinating the review of this manuscript and approving it for publication was Santi C. Pavone.


This work is licensed under a Creative Commons Attribution 4.0 License. For more information, see https://creativecommons.org/licenses/by/4.0/

broadband [29], [30]. A broadband near-perfect MMA in the solar spectrum generally consists of a three-layer structure with metal-dielectric-metal (resonator) layers. The metal layer halts the transmission of the electromagnetic (EM) wave, and the dielectric layer helps the structure to create a coupling capacitance between the metal and the resonator layer [31]–[33]. However, these may not be the only reasons for a near-perfect MMA. Perfect impedance match of the metal with the free space of the solar spectrum [34], [35], the plasmonic resonance characteristics of the dielectric layer [36], [37], a symmetrical structure resonator with good confinement of the EM wave [38], [39], and a good E-field, H-field and distributed surface charge are also reasons for high absorption [40], [41]. MMA may also consist of two-layer [42], four-layer [43], [44], multilayer stacks [45]–[47] along with most common three-layer structure. As a result of the periodic structure of the artificial design of MMAs, they show high absorption with a wide wavelength even though they are ultrathin [48]–[50]. Broadband MMA was first discussed by Lee *et al.* in 2012 with FR4 and copper in the GHz frequency region [51]. After that, broadband MMA in the optical region was also demonstrated by many types of research until today. Some of them are discussed below with the results the studies found, the materials they used, and their angular and polarization stability.

A multi-circular PMA with Al-GaAs-Al with three near-unit absorption peaks for TE and TM polarization in both the visible and near-infrared (NIR) regions [52]. A four-layer polarization-independent plasmonic metamaterial absorber based on nanocomposite ($SiO_2$/Gold) found above 85% absorbance from the 400nm to the 750nm wavelength [53]. An average absorption above 95% had been achieved with a three-layer MMA consisting of TiN-$SiO_2$-TiN for the full visible region at TE and TM mode. Here TiN was used as a refractory plasmonic material [54]. A unique three-layer MMA was proposed by C. Tun *et al.* with a phase-change material ($Ge_2Sb_2Te_5$) layer along with gold as a metal for NIR and the visible wavelength. They found two-peak absorption at 96.8% and 96.2% at 610nm and 870nm, respectively [55]. S. Cao *et al.* used a meta-nanopillar array consisting of Au/Si to achieve an average 96% absorbance for the whole visible wavelength with 60° angular stability for both TE and TM polarization [56]. A silicon-based MMA with conical and circular holes with Au as the metal and a dielectric layer of $SiO_2$ had absorption above 80% from 437.9nm to 578.3 nm with peak 98.2% absorption. It had angular stability up to 60° [57]. An MMA based on a metasurface formatted with a sandwiched metal-dielectric-metal layer found a peak of 92% absorption in the optical wavelength, with an average of an 83% absorption value [58]. Si- and Ni-based MMAs can be applicable with above 90% absorption for the optical wavelength and above 99% from 500nm to 560nm [59]. A genetic algorithm (GA)-based MMA consisting of Au-$SiO_2$-Au had above 90% absorption with 40° angular stability for TE and TM polarizations [60]. An MMA with an arbitrary cutting top layer with quartz substrate with two gold layers had above 80% absorption from 575nm to 760nm with four near-unity peaks [61].

MMAs also can be found in IR [62], UV [63], THz [64], GHz [65], MHz [66], KHz [67], Hz [68] with visible/optical region as discussed above with applications like STPV [69], light trapper [70], cryptography [71], thermal detector [72], sound absorption [73], underwater sound absorption [74], detectors [75], military radar devices [75], detection of explosives [76], photonic circuit [77], filter [78], refractive index sensor [79], reflector [80], thermal imaging [81], antenna [82], light detection [83], [84], energy harvesting [85], [86], imaging [87], [88], sensors [89]–[91].

Inspired by previous work with numerous applications in the related field, an MMA for the whole optical region has been proposed here. From the earlier literature review, it can be seen that an MMA with an average absorption up to 95% is not highly obtainable with a comprehensive incident angle like 50° and up for TE and TM mode. Also, it is also known that the optical region is the primary source of the sun's electromagnetic emission (EM) waves. Another paramount and common problem that arises with an MMA for optical use is temperature stability, as electromagnetic emissions of the solar spectrum are very high, which creates excessive temperatures. To eradicate this type of problem, the proposed MMA uses an excellent symmetrical structure, with high-temperature solid materials, namely tungsten and silicon dioxide. The design shows 96.7% absorptivity for the optical region and 90.28% for the ultraviolet–optical–near-infrared region. It has a near-unity absorption level of 99.99% at 498.25% and above 99% from 460nm to 540nm. The key explanation for the strong absorption is a reasonable impedance match, along with other purposes discussed later. The design is simulated, and the simulated results were proved by the interference theory model (ITM) for the whole region. Various parametric analyses and changes in dielectric and metal help to optimize the design. As it has been known that the optical region is the main source of the sun's EM waves, these forms of MMAs will open up a new age with specific implementations for the relevant sector.

## II. DESIGN AND SIMULATION SETUP

### A. MATERIALS CHOICE

As the proposed MMA structure works in the optical wavelength, it is crucial to choose metal and dielectric layers with high-temperature stability and proper optical properties. Innumerable materials options that can be used in a three-layer structure are shown in Fig. 1, regarding wavelength with the help of various literature reviews on recent works. Only ultraviolet (UV)-optical (OPT)-near infrared (NIR) regions shown here for less complexity.

The proposed structure uses tungsten (wolfram [w]) (optical, Palik) as a metal and resonator layer and lossless silicon dioxide ($SiO_2$) (optical, Ghosh) with invariant - refractive index of 1.5 at the full visible wavelength as the dielectric layer. The optical properties of the W and $SiO_2$ with

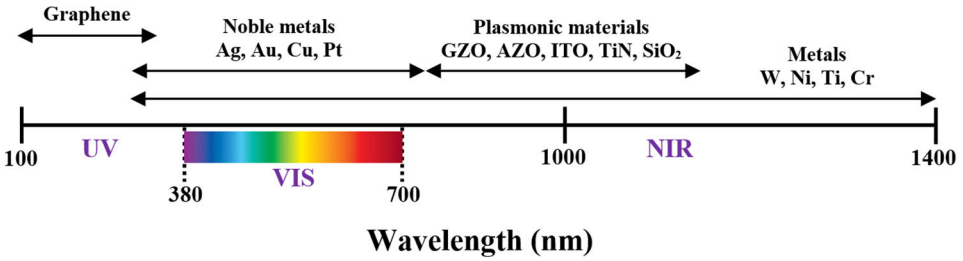


**FIGURE 1.** Understanding the choices of materials (not limited to) when designing an MMA for UV-OPT-NIR regions.

dispersion equation and band structure are given in [92], [93]. A perfect impedance match with free space in the optical region of tungsten is the main reason for choosing it as a metal and resonator layer with its high intrinsic losses. Tungsten itself is also an excellent absorber on its own with a low ohmic loss. High temperature stability (3422 °), however, often renders tungsten the best choice for metal for MMAs in the optical wavelength region. Lossless resonance characteristics help $SiO_2$ to achieve a good impedance match with the free space of the optical region, with a large imaginary part for a wide range. As the dielectric layer helps the structure to create a suitable coupling capacitance and inductance with the resonator and metal layer, its low refractive index (1.5) helps the structure acquire higher absorbance with a larger bandwidth. $SiO_2$ also has a very high melting point (1710 °), which will help the structure withstand a very high electromagnetic waveform of the solar structure.

### *B. DESIGN OF THE UNIT CELL STRUCTURE*

Encapsulating a good absorption with near-unity is highly dependent on the physical dimension of a structure and the resonator. Many resonator structure like helix-shape [94], saw tooth [95], tapped array [96], circular-sector [97], hourglass-shape [98], coin-shaped [99], arrow-shaped [100].

From Fig. 2, (a)-(d) the progressive development of the design of the unit cell is exhibited step by step. In Fig. 2, (e) and (f) the physical dimension of the proposed structure can be perceived with the front-view and the side-view from the x-axis, respectively. From Table 1, the parameters of the structure can easily be understood. The most common three-layer sandwiched design with metal-dialectic-metal and a unique symmetrical-shaped resonator (SSR) is used in this structure. First, the back-layer and dielectric layer are implemented in the design with a total length and width of "a = 1000nm". Here, the back-layer (metal) thickness was "tm = 150nm" and the dielectric layer thickness was "td = 60nm". The back-layer metal thickness was greater than the skin depth, $(\delta) = (2\rho/2\pi f \mu_R \mu_0)^{1/2}$ to guarantee near-zero transmission in the full optical region. Then in step 1, four symmetrical shapes in four directions were applied with length "rl = 750nm" seen in Fig. 2(a). In step 2, a square box was added with the previous symmetrical shape shown in Fig. 2(b). And then, in step 3, a circular

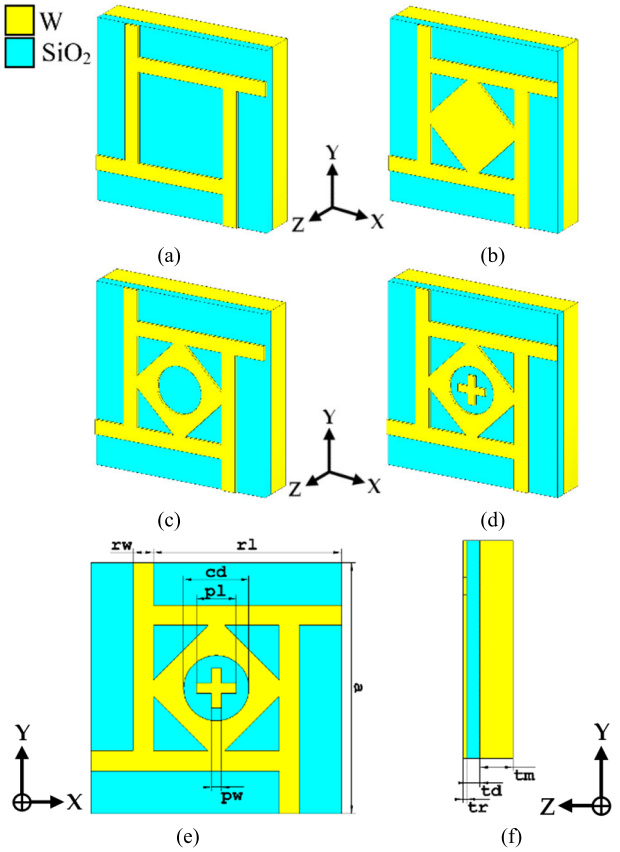


**FIGURE 2.** Design procedure of the proposed unit cell with three dimensional view of (a) step 1, (b) step 2, (c) step 3, and (d) final proposed design along with axis. Physical dimension of final design with (e) front view, and (f) side view with axis.

cuts in the resonator with a diameter of "cd = 260nm" has been made, which is visible in Fig. 2(c). For the final step, a cross shape with a length of - "pl = 160nm" and a width of "pw = 40nm" was added inside the cylindrical cut, thus completing the proposed structure, as demonstrated in Fig. 2(d). The resonator layer thickness was "tr = 15nm". This design is a rational, symmetrical structure as will be proved below with sufficient data. Note that the total thickness of the unit cell is 225nm, which is ultrathin. These types of ultrathin structures can be easily rolled over to any solar thermo-photovoltaic (STPV) cell. Also note that tungsten is shown as yellow and silicon dioxide as cyan in Fig. 2.

**TABLE 1.** Parameter list of the proposed unit cell design with value in nm.

| Parameters | Value (nm) |
|---|---|
| a | 1000 |
| tm | 150 |
| td | 60 |
| tr | 15 |
| rl | 750 |
| rw | 80 |
| cd | 260 |
| pl | 160 |
| pw | 40 |

### C. SIMULATION SETUP

To gain the desired absorption level from scattering parameter, it is essential to have the correct simulation setup with good boundary conditions. Boundary conditions are used to restrict approaches for the electromagnetic amounts correlated with this. In this design for the transverse electromagnetic (TEM) mode, periodic boundary condition with the perfect electric conductor (PEC) and the perfect magnetic conductor (PMC) were taken from the x-axis and y-axis respectively. For the PEC, the electric field is asymmetrical and the magnetic field is symmetrical, while for the PMC the fields are vice versa. The operating wavelength source will pass through the z-axis as it was considered as open space with a perfectly matched layer (PML) in the negative direction which also abolish scattering. All three axis are perpendicular to each other in the setup. Linearly polarized planar wide-spectrum wave incidence on the planned absorber's top surface for simulation. For transverse electric (TE) and transverse magnetic (TM), the floquet port is used in the z-axis, with the master and the slave being in the x-axis and the y-axis, respectively. In order to render the simulation results more precise, a higher mesh order is used. All the data were simulated in the computer simulation technology microwave studio (CST MWS) based on the finite integration technique (FIT). Frequency-domain analysis has been used to acquire all the data. Data refinement was done with the CST-MATLAB interference.

## III. RESULTS ANALYSIS AND DISCUSSION

### A. METHODOLOGY FOR CALCULATION OF ABSORBANCE

For calculation of absorbance, scattering parameters (S-parameter) are extracted by the Nicolson–Ross–Weir (NRW) method discussed in reference [101]. As absorbance is highly dependent on the impedance match, the impedance of the unit cell $Z(\omega) = \{\mu_r(\omega).\mu_0/[\varepsilon_r(\omega).\varepsilon_0]\}^{1/2}$ and characteristic impedance $Z_0 = (\mu_0/\varepsilon_r)^{1/2} = 376.73 \approx 377\Omega$. Where, $\mu_0$ = permeability of free space, $\varepsilon_0$ = permittivity of free space, $\mu_r$ = relative permeability, and $\varepsilon_r$ = relative permittivity. By calibrating the physical dimensions of the design, condition ($Z(\omega) = Z_o$), can be achieved, and the design will give almost unity absorption at a wavelength as it highly depends on wavelength. Here, $Z(\omega)$ is $Z_o$ very close to the desired value; if we can equal the value, and design may be act as a super absorber with unity absorption. As absorption is inversely proportional to the reflection and the transmission coefficients, the absorption formula will be,

$$\begin{aligned} A(\omega) &= 1 - R(\omega) - T(\omega) \\ &= 1 - |S_{11}(\omega)|^2 - |S_{21}(\omega)|^2 \end{aligned} \quad (1)$$

Here, R($\omega$) is the linear value of s-parameter $S_{11,}$ which is also called the reflection coefficient, and T($\omega$) is the linear value of the $S_{21}$ parameter, which can also be called the transmission coefficient. However, the high thickness of tungsten blocks almost all the EM waves, which is why T($\omega$) can be rewritten as near zero. So the final absorption formula will be,

$$A(\omega) = 1 - R(\omega) = 1 - |S_{11}(\omega)|^2 \quad (2)$$

### B. ABSORPTION CHARACTERISTICS

Figure 3(a) manifested the absorption characteristics for transverse electromagnetic (TEM), transverse electric (TE), Transverse (TM), from wavelengths of 300nm to700nm, using the metal and resonator as tungsten and the dielectric layer as silicon dioxide. These characteristics are calculated from (1) or (2) using the s-parameter attained from the simulation. This design shows an excellent absorbance for all three modes from the ultraviolet–optical–near-infrared region. For the TEM mode, absorption consists of an outstanding level at 300nm–1000nm at 72% and 73.36%, respectively, with an average absorption of 90.28%. A near-unity peak is found at 498.25nm with 99.99% absorbance. As the design is a very good symmetrical design, the TE and TM modes find almost the same absorption level with an average absorption of 90.22% for a large bandwidth of 700nm. However, despite a high absorption in the UV–OPT–NIR region, we will focus only on the optical region for all the sections discussed below, as it is considered to be the most important region to work with. We will consider the optical region from 380nm to 700nm as it is appraised as the standard. The structure finds an average absorption of 96.7% in the TEM mode, starting at 92.64% and ending at 91.6% from 380nm to 700nm, respectively, with near-unity absorption at 498.25nm. The TE and TM modes find average absorption of 96.61% with a 99.99% absorption level. The absorbers show up to 96.72% day-integrated solar energy absorption, which is 32% better than with loss-induced semiconductor/metal absorbers.

For a better understanding of the phenomenon of absorption, the design was divided into two different layers. One is the back-layer, which is only the metal layer, and another is the front-layer, which consists of the metal resonator and the dielectric. Absorption with the front-layer and the back-layer is shown in Fig. 3(b). From the figure, it is realized that the back-layer absorbs almost half of the absorption. Because the

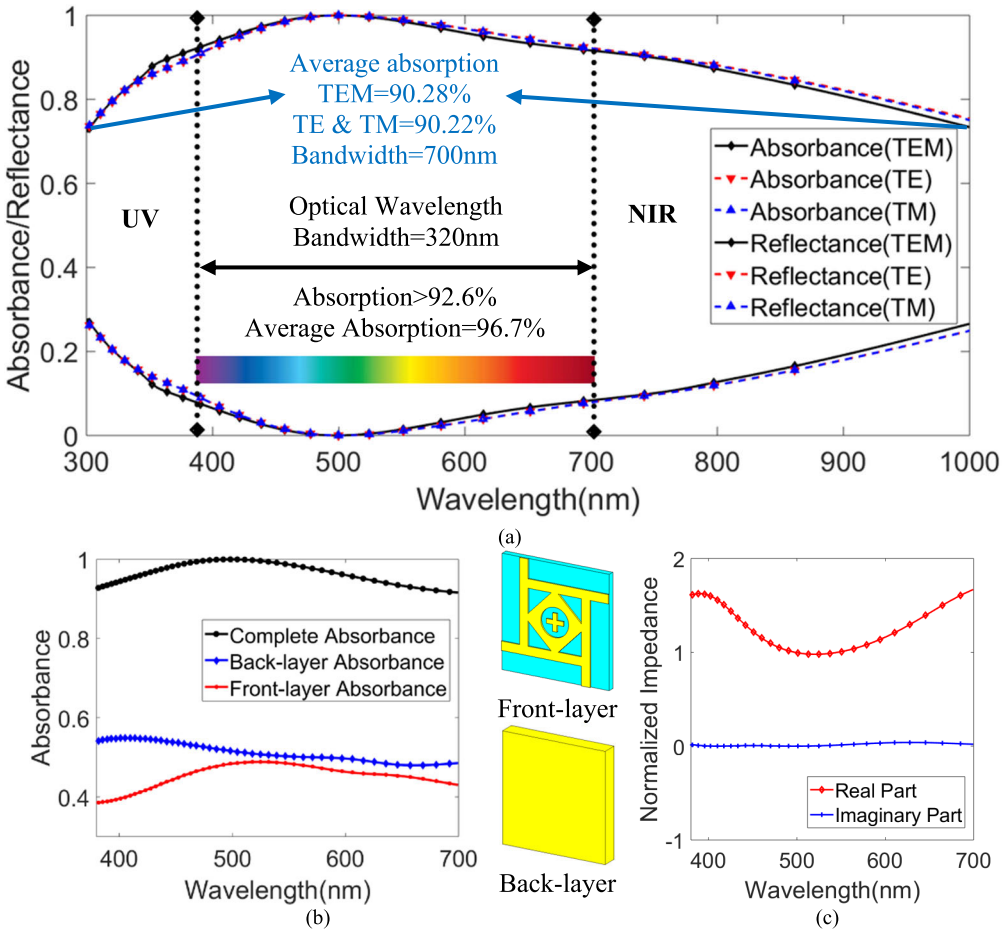


**FIGURE 3.** Graphical representation of (a) absorbance and reflectance of TEM, TE, and TM mode from wavelength 300-1000nm, (b) absorbance evaluation with front-layer and back-layer with visual portrayals, and (c) normalized impedance with real and imaginary parts.

design used tungsten as a back-layer, it is known that surface plasmons do not operate in tungsten in the optical region, so it examined outstanding impedance match with the free space of the same region. However, the front-layer also helps the structure to achieve the impedance match. As silicon dioxide shrinks the distance from the resonator to the metal with a shallow thickness of 60nm, it creates resonance characteristics. The resonator layer's intrinsic losses are also a reason for the high impedance match. For a high impedance match, real parts of the normalized impedance must be close to zero, where the imaginary parts must remain near zero. These two phenomena were achieved by the unit cell design, which can be easily seen from Fig. 3(c). Also, an excellent coupling capacitive and inductance value consists of the metal, and the resonator layer with the help of dielectric is a major reason too for the good absorption in the whole region with a near-unity peak. However, these phenomena may not be able to capture the fallen wave if the resonator is not a symmetrical resonator with an excellent design. Four symmetrical shapes with plus-shape circular cuts imprison the electromagnetic wave as it reflects the wave with the back-layer from the front end with complex dispersion and confines it in the dielectric layer.

### C. CO-POLARIZATION AND CROSS-POLARIZATION WITH POLARIZATION CONVERSION RATIO (PCR)

The absorption curve is acquired from (1) and (2), as shown above. But one question still arises for an MMA that the unit cell must not work as a polarization converter and give the PCR value instead of the absorption. The structure is symmetrical, but to clinch the matter, we demonstrated both co-polarization and cross-polarization components in Fig. 4(a) with the help of (3) and (4). From Fig. 4(a), it can be easily seen that the cross-polarization component is almost zero in the linear magnitude scale, and this ensures that the design did not convert the waves in the scrutinized wavelength region.

$$|S_{11}(\omega)|^2 = |S_{TE,TE}(\omega)|^2 + |S_{TE,TM}(\omega)|^2 = R_{yy}^2 + R_{yx}^2 \quad (3)$$

$$|S_{11}(\omega)|^2 = |S_{TM,TM}(\omega)|^2 + |S_{TM,TE}(\omega)|^2 = R_{xx}^2 R_{xy}^2 \quad (4)$$

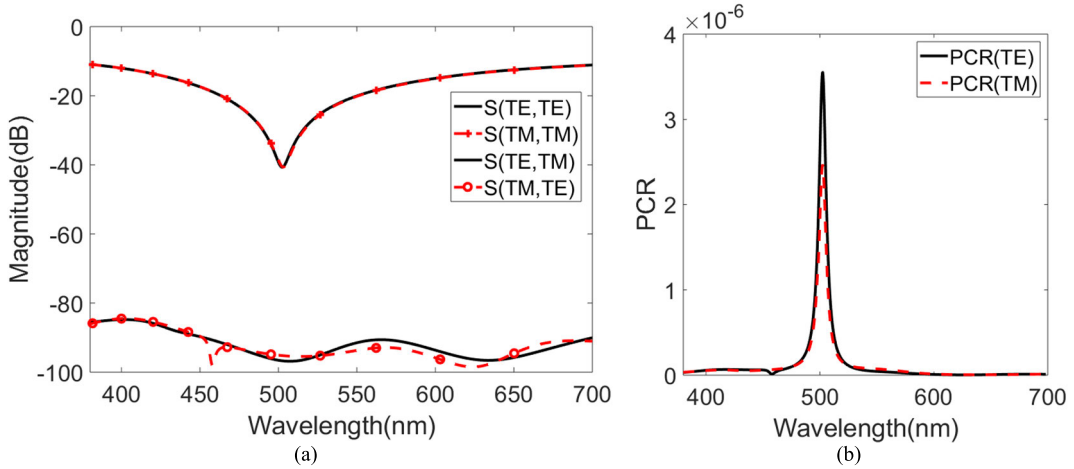


**FIGURE 4.** Co-polarization and cross-polarization magnitude (dB) of the reflection coefficient ($S_{11}$) for (a) TE and TM-polarization mode, and (b) polarization conversion ratio (PCR) of the proposed unit cell for both TE and TM mode for the visible region.

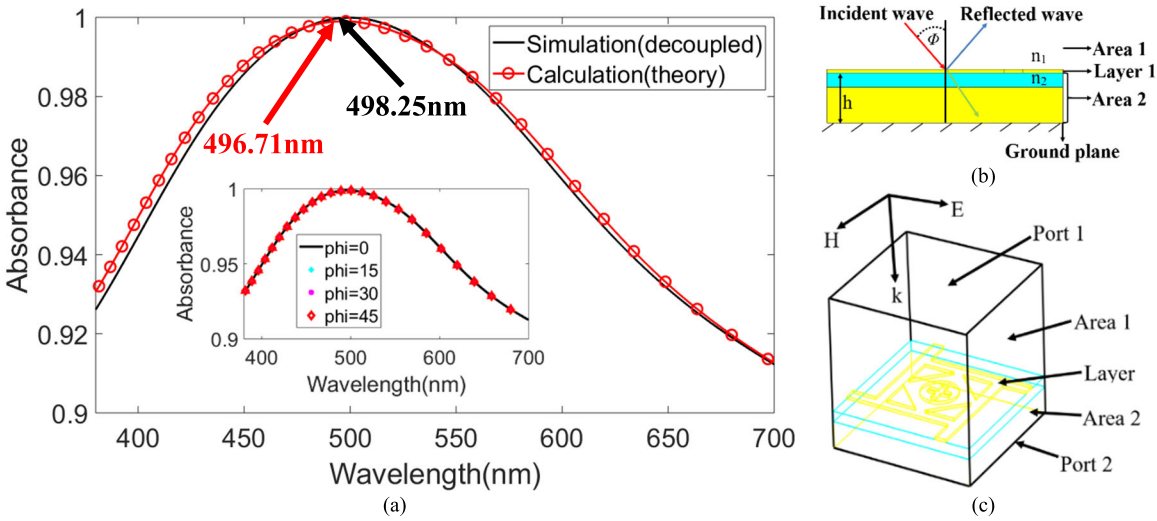


**FIGURE 5.** Graphical representation of (a) Comparison of absorbance with the calculated investigation, a schematic diagram of (b) interference theory model with different incidence angle, and (c) the decoupled-model (MMA unit cell without a ground plane). Insets (a): absorbance for different oblique polarization angle.

here, $|S_{TE,TE}(\omega)|^2 = |S_{TM,TM}(\omega)|^2 = R_{yy} = R_{xx}$ = co-polarization reflectivity and $|S_{TE,TM}(\omega)|^2 = |S_{TM,TE}(\omega)|^2 = R_{yx} = R_{xy}$ = cross-polarization reflectivity.

In addition, the PCR of the cell can be calculated by (5) or (6), which can be observable from Fig. 4(b). The PCR value of the proposed design is near zero for both TE and TM mode, which eliminates the matter of polarization conversion characteristics entirely.

$$PCR_{TE} = R_{yx}^2/(R_{yy}^2 + R_{yx}^2) \quad (5)$$

$$PCR_{TM} = R_{xy}^2/(R_{xx}^2 + R_{xy}^2) \quad (6)$$

### D. THEORETICAL VERIFICATION

Verification of simulated result with the interference theory model discussed in this section for normal and oblique angles from 0° to 45°. For the verification, decoupled simulated data were compared with the calculated data acquired from the interference theory model. The comparison graph is given below in Fig. 5, with the schematic model in Fig. 5(b) and the decoupled model in Fig. 5(c). According to interference theory from the references [102]-[104], with the ground plane, total reflection $S_{11total}$ for layer 1 can be calculated from (7).

$$\begin{aligned} S_{11total} &= S_{11} + S_{12}e^{-}j\beta e^{-}j\pi e^{-}j\beta S_{21} \\ &\quad + S_{12}e^{-}j\beta e^{-}j\pi e^{-}j\beta(S_{22}e^{-}j\beta e^{-}j\pi e^{-}j\beta)^1 S_{21} \\ &\quad + S_{12}e^{-}j\beta e^{-}j\pi e^{-}j\beta(S_{22}e^{-}j\beta e^{-}j\pi e^{-}j\beta)^2 S_{21} + \cdots \\ &= |S_{11}|e_{11}^{j\theta} + ((|S_{12}||_{S21}|e^{j(\theta 12+\theta 21-2\beta-\pi)})/(1 \\ &\quad - |S_{22}|e^{j(\theta 22-2\beta-\pi)})) \end{aligned} \quad (7)$$

here, $S_{11} = |S_{11}|e_{11}^{j\theta}$, reflection coefficient for layer 1 from area 1 to 2

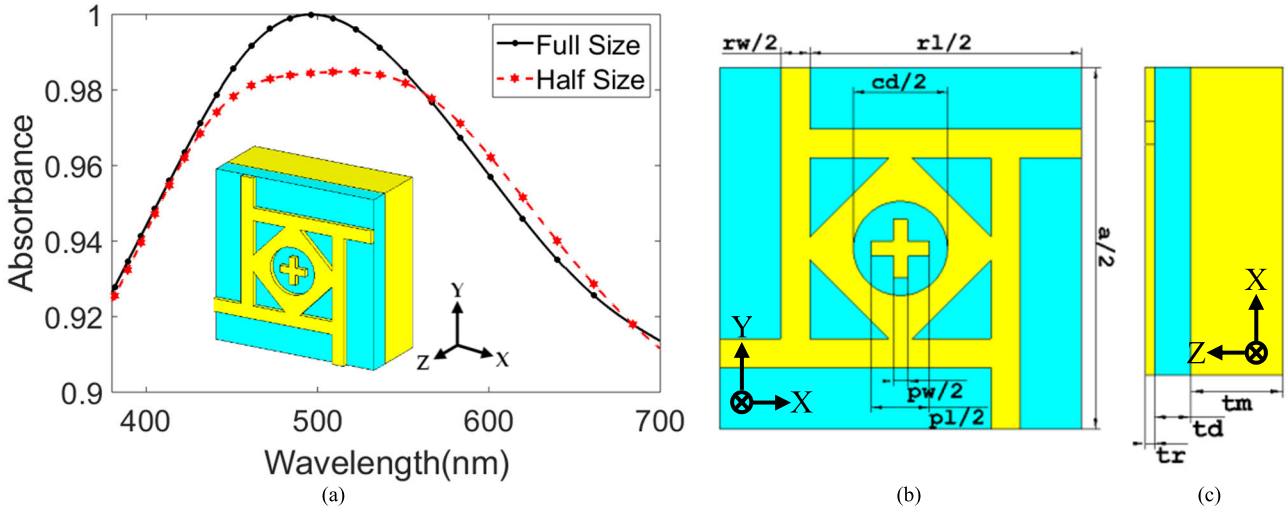


(a) (b) (c)

**FIGURE 6.** Absorbance comparison with half of the proposed unit cell size (a) Comparison graph, (b) front view of the half-size structure, and (c) side view of the half-size structure with the axis. Insets (a): 3D dimensional view of the half of the structure with the axis.

$S_{21} = |S_{21}|e^{j\theta}_{21}$, transmission coefficient for layer 1 from area 1 to 2

$S_{12} = |S_{12}|e^{j\theta}_{12}$, transmission coefficient for layer 1 from area 2 to 1

$S_{22} = |S_{22}|e^{j\theta}_{22}$, reflection coefficient for layer 1 from area 2to 1

And, $\beta = kd$

Where, $\beta$ = complex propagation phase, $k$ = wave number in are 2, d = propagation distance

The above discussion proved that the design is symmetrical. So, $S_{12} = S_{21}$. Then we can rewrite the equation (7), in (8).

$$S_{11total} = |S_{11}|e^{j\theta}_{11} + ((|S_{12}|^2 e^{j}(2\theta 12 - 2\beta - \pi)/(1 - |S_{22}|e^{j(\theta}_{22} - 2\beta - \pi)) \quad (8)$$

Finally, the absorption can be theoretically calculated from the simple equation $A(\omega) = 1 - |S_{11total}|^2$, using 3 and 4, here the back layer obstructs the transmission, so $T(\omega) = 0$.

From Fig. 5(a), we can easily realize that the simulated value of absorbance is very close to the calculated absorbance from the interference theory we discussed above. Both of the results demonstrate an excellent absorption level with peak values above 99.9% and with average absorption of 96.72% and 96.90% for simulated and calculated results, respectively. These results will help to verify the proposed design under normal conditions.

### E. ABSORPTION OF HALF OF THE UNIT CELL STRUCTURE

A unique feature of the proposed design is discussed here. When the scale of the suggested unit cell configuration y-x axis parameters is half as large as the real structure, the model also exhibits an outstanding average absorption level of 96.25% with a peak of 98.24% in the full optical region, which can be easily seen from Fig. 6a-c. As it is understood, a metamaterial unit cell may be rendered considerably smaller than the free space of the wavelength and considerable phase variance at practical operating frequencies [105]. This is the main reason why such absorption has occurred for the structure. Here, the thicknesses of the resonator, dielectric, and metal layers are unchanged. When the small structure size is considered, the design may be used with half of the size.

### F. POLARIZATION AND INCIDENT ANGLE STABILITY

As mentioned earlier, the structure is wide-angle stable for both the TE and the TM modes. In this study, the performance of the MMA with the various oblique incidences of the TE and TM waves are discussed. From Fig. 7(a) and (b), it can be seen that the design is entirely polarization angle sensitive from 0° to 90° because of its symmetrical structure, which was proved above. However, an ideal MMA must also be stable for the incident angle to use it as a solar cell, or for energy harvesting, as a solar sensor or a detector, or for many other important applications.

Figure 7(c) demonstrate the design from 0° to 60° with the increments of 10° for the various incident angles in TE mode. Here, the unit cell shows minimal alteration, and we find average absorption of above 82.17% for all incident angles, with peak absorption of 70%. As the path length of the wave is directly proportional to the angle of incidence, the higher the angle, the higher the path length. Because of the long path, the coupling effect of the resonator and metal decreases for the weaker magnetic dipolar resonance. Confinement of the wave in the dielectric layer is affected by the phenomenon and creates lower absorptivity.

A different scenario occurs for the TM mode exhibited in Fig. 7(d) from the TE mode we discussed above. We have better stability with average absorptivity, which changes from 96.61% to 94.15% for the incident angle of 0° to 90° this time.

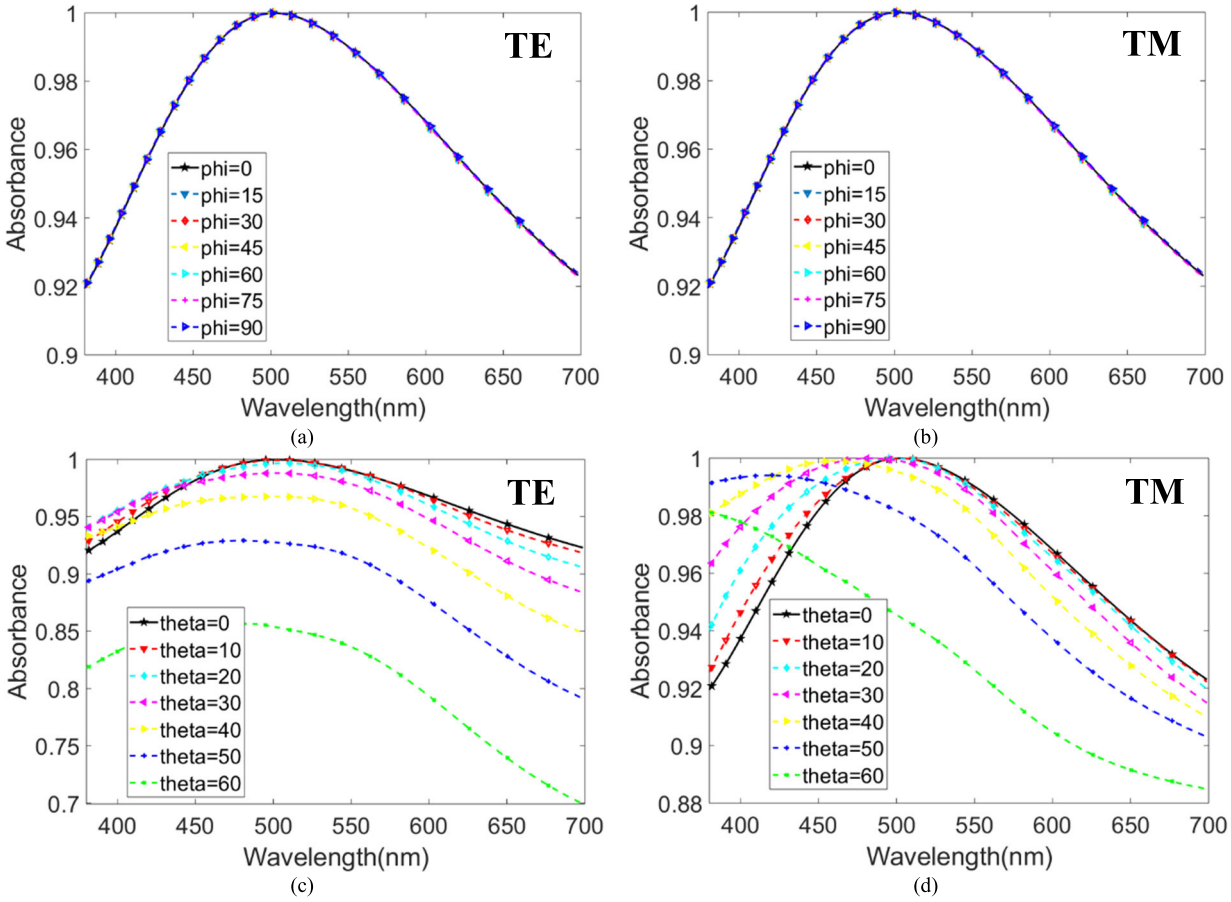


**FIGURE 7.** Graphical representation of absorbance for different polarization angle (phi) from 0-90° for (a) TE mode, (b) TM mode, and different incident angle (theta) from 0-60° for (c) TE mode, (d) TM mode.

The MMA absorptivity level does not change as much as with the incident angle in the TM mode. The larger electric field concerning the perpendicular incident angle rather than the parallel component is the reason for better stability in the TM mode. Excellent coupling with good confinement of the wave makes this design a polarization- and incident-angle stable MMA, which enriches its application criteria for many fields.

### G. GEOMETRIC PARAMETER SWEEP

Table 1 showed that the structure used nine parameters when it was designed. Geometric shape highly depends on the parameters, and absorption depends on the geometric structure. The most important parameter sweep has been discussed here, which showed in Fig. 8.

First of all, the parameter ''a'' has been changed from 1000nm to 1200nm, which will increase the length and width of the back-layer and dielectric layer proportionally. This parameter sweep will make sure the matter that, when the resonator fit with the dielectric and metal layer, the design exhibited the highest average absorption value shown in Fig. 8(a). However, average absorption is almost near 96.70% for all value of ''a'', but the resonant absorption finds with the value ''a = 1000nm''. Another parameter sweep demonstrated in Fig. 8(b) where the width of the outer side of the resonator has been changed from 50nm to 110nm. Also, here, not an immense variation occurred with the average absorption, which maintained an excellent level around 96.6%. But, the resonant absorption is found with ''rw = 80nm''.These two phenomena happened as the self and mutual inductance changes with the sweep of the parameter. Successive increment of ''a'' and ''rw'' increase the mutual inductance but decreased the self-inductance which produces with the metal and the resonator layer. That's why the resonance wavelength decreased with both of them. These two parameter sweeps also help to find the best geometric design with high absorption.

A major and important sweep with parameter ''td'' takes place here. Here the dielectric layer thicknesses increased by a step of 10nm from 40nm-80nm, which initiate very imp important exhibited in Fig. 8(c). Here, resonant wavelength increased linearly at 405.23nm, 442.17nm, 498.25nm, 558.51nm, and 620.64nm for 40nm-80nm width of the dielectric layer respectively. Here peak absorption is changes with 98.07%, 99.77%, 99.99%, 99.94%, and 99.93%. As the structure irradiated by an EM wave, it creates capacitance with the metal layer and resonator with the help of the dielectric layer.

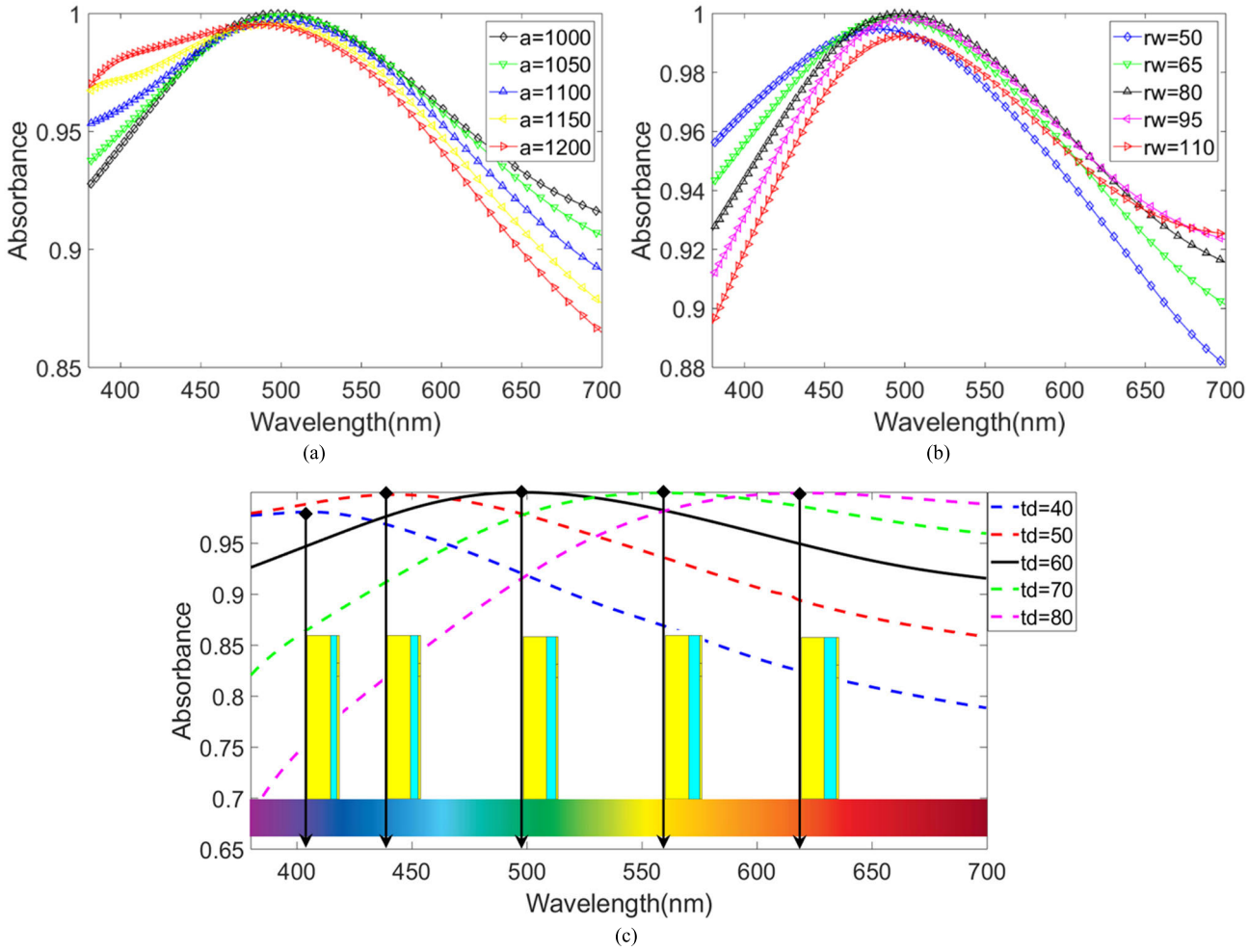


**FIGURE 8.** Parametric sweep of (a) parameter "a", (b) parameter "rw", and (c) parameter "td" with a graphical and visual representation for TEM mode.

However, the capacitance of a structure highly depends on the dielectric thickness and inversely proportional to it. Successive increment of the thickness has decreased the capacitance; hence the resonant wavelength shifted from left to right linearly. With this important phenomenon, this structure may be used as an optical sensor, dielectric layer thickness sensor. Also, the dielectric layer confined most of the wave within it and made a structure highly procurable for absorption. So, a maintained thickness of dialectic is a must for good absorption. Here we select the thickness of the dielectric at 60nm after completing the parameter sweep with different thicknesses.

### *H. ABSORPTION COMPARISON WITH DIFFERENT DIELECTRIC LAYERS AND METALS*

Here, we simulated our design with some dielectric layer and metal (resonator and back-layer) choices. Fig 9 and 10 ensure that the choice of tungsten with silicon dioxide is perfect. However, as it is known that a high absorption level is not always a must for application, some other applications have been discussed here with different dielectric or metal layers.

First, the dielectric substance was changed with four different materials along with silicon dioxide and exhibited in Fig. 9. The new materials are gallium arsenide (GaAs), silicon nitride, graphene, and amorphous silicon. Here we can see that silicon dioxide gives far better average absorption than the other materials. The reason for this kind of variation is the different refractive indices of those materials. As we know, the lower the refractive index, the higher the absorption and the more extensive the bandwidth. The refractive indices of $SiO_2$, GaAs, graphene, $Si_3N_4$, and A-Si are 1.5, 3.9, 2.6, 2.0, and 4.4, respectively. However, as the absorption level was linearly increased with $Si_3N_4$, it can be used as a light detector for the visible regime. And GaAs and A-Si can be used as half-power absorbers as they exhibited half-absorption level for almost the full region.

Finally, the unit cell was simulated with different metals, namely aluminum, copper, platinum, and silver along with tungsten, as shown in Fig. 10. A good impedance

**TABLE 2.** Comparison of proposed unit cell with various previous work with similar features and relatively close bandwidth.

| Range (nm) | layer | Dimensions (nm) | Materials | Polarization -insensitive | Angular stability for Up to 70% Absorption | Absorption level | Peak Absorption | validation | Ref. # |
|---|---|---|---|---|---|---|---|---|---|
| 262-709 | Two | 240×240×170 | Au, Si | Yes | $\theta \leq 50°$ | Above 90% | 99.1% | Simulated | [42] |
| 430-1400 | Three | 690.5×90.5×410 | Al, GaAs | Yes | Not mentioned | Not a broadband MMA | Three peaks with 99.99% | Simulated | [52] |
| 400-750 | Four | Nanocomposite with Width = 250 | $SiO_2$-Au composite, $SiO_2$, Au, Glass | Yes | $\theta \leq 60°$ | Above 85% | 99% | Simulated & measured | [53] |
| 400-800 | Three | 300×300×240 | TiN, $SiO_2$ | Yes | $\theta \leq 50°$ | Above 87% | 99% | Simulated & measured | [54] |
| 400-700 | Thirty-two layer array | Nanocomposite with Width = 300 | Au, Si | Yes | $\theta \leq 60°$ | Above 91% | 99.95% | Simulated | [56] |
| 437.9-578.3 | Three | 300×300×272 | Au, $SiO_2$, Si | Yes | $\theta \leq 80°$ | Above 80% | 98.2% | Simulated | [57] |
| 470-810 | Three | Nanocomposite with Width=147 | Au, $SiO_2$, $SiO_2$-Ag composite | No | N/A | Above 80% | 93% | Simulated & measured | [58] |
| 400-700 | Three | 800×800×355 | Ni, Si | Yes | $\theta \leq 60°$ | Above 90% | 99% | Simulated & measured | [59] |
| 430-850 | Three | 320×320×50 | Au, $SiO_2$ | Yes | $\theta \leq 40°$ | Above 90% | 99%% | Simulated & optimized | [60] |
| 575-750 | Four | 500×500×240 | Ai, Kerr | Yes | $\theta \leq 40°$ | Above 80% | 99% | Simulated | [61] |
| 400-850 | Three | 500×500×174 | Al, $SiO_2$ | No | N/A | Not a broadband MMA | Two peaks with 92% & 99.99% | Simulated & measured | [109] |
| 300-750 | Four | Nanocomposite with Width = 250 | Ag, $SiO_2$, $SiO_2$-Ag composite | No | N/A | Above 90% | 99.8% | Simulated & measured | [110] |
| 400-750 | Three | Nanocomposite with Width = 182 | Au, $SiO_2$, Al | Yes | $\theta \leq 60°$ | Above 80% | 99% | Simulated & measured | [111] |
| 380-700 | Three | 1000×1000×225 | W, $SiO_2$ | Yes | $\theta \leq 60°$ | Above 91.6% | 99.99% | Simulated & calculated | This work |

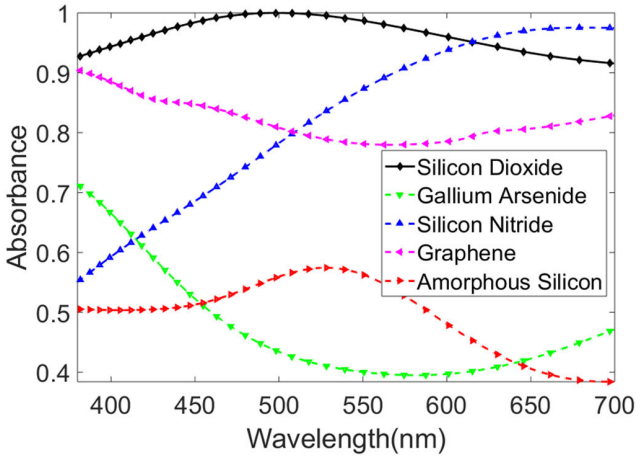


**FIGURE 9.** Comparison of absorbance with different types of the dielectric layer.

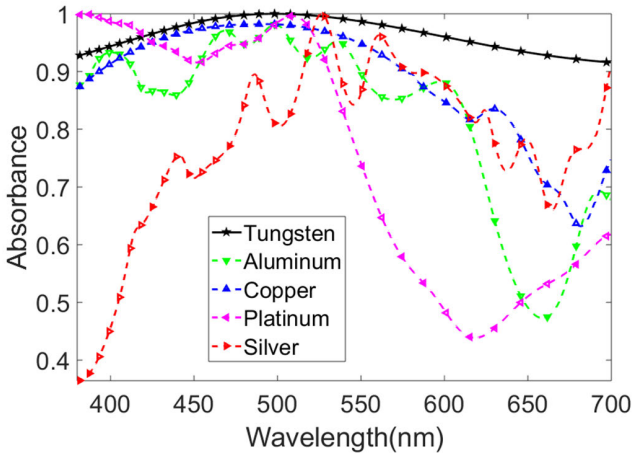


**FIGURE 10.** Comparison of absorbance with different types of the metal.

match of tungsten with a full optical region makes it perfect for the proposed cell. Here platinum and copper indicate a good absorption level from 380nm to 500nm and 980 to 575nm, respectively, with above 90% absorption. Thus, they can be used as a wideband absorber for various applications. Aluminum and silver didn't show proper absorption as they didn't match the desired impedance with this particular structure.

### I. E-FIELD, H-FIELD AND SURFACE CURRENT DISTRIBUTION

Absorption characteristics depend on the electromagnetic field and surface charge distribution for both TE and TM

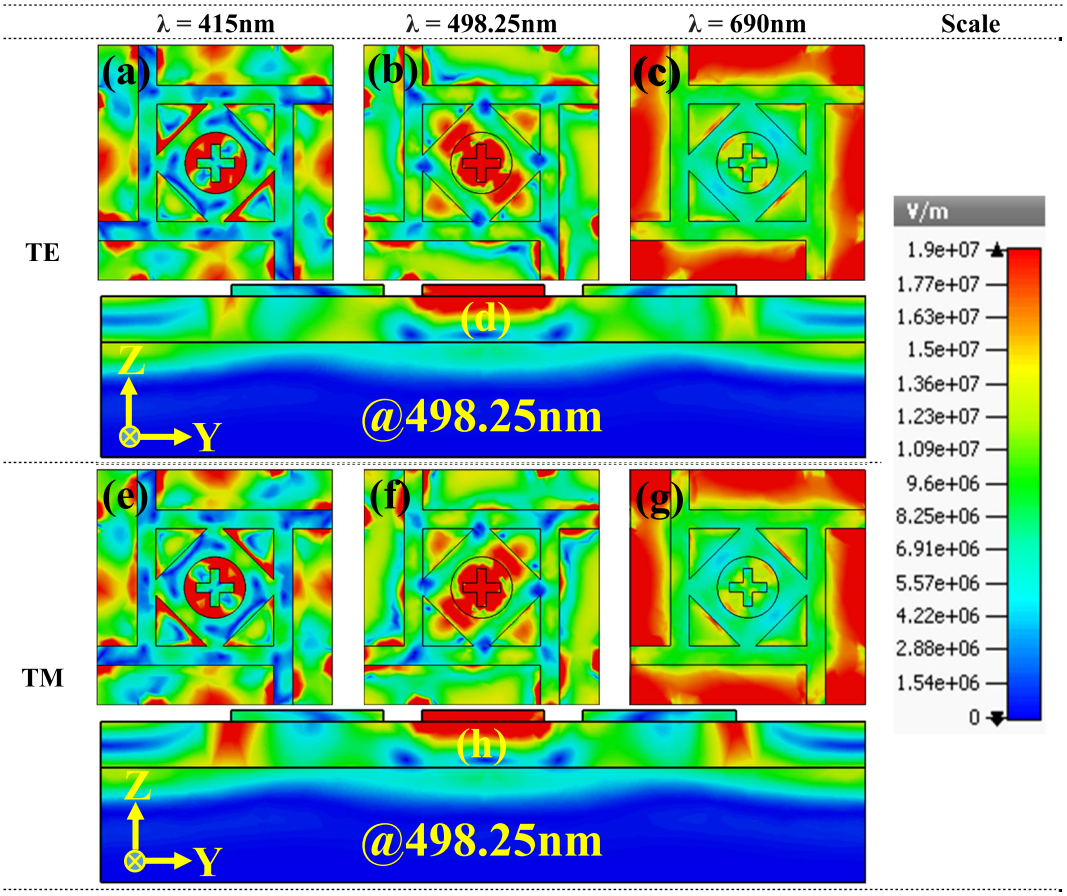


**FIGURE 11.** Representation of electric-field distribution of the unit cell (a)-(c) for TE polarization in 415nm, 498.25nm, and 690nm with linear color bar ($Vm^{-1}$) in y-x axis, (d) cross-sectional view of the middle of the structure at 498.25 (peak) resonance wavelength in z-y axis, (e)-(g) TM polarization in 415nm, 498.25nm, and 690nm with the same linear color bar ($Vm^{-1}$) y-x axis, (h) cross-sectional view of the middle of the structure at 498.25 (peak) resonance wavelength in z-y axis for normal incidence angle.

mode. As described above, the magnetic dipolar moment created for the metal resonator and the back-layer created the resonance in the dielectric layer. Thus, the absorbance is mainly confined in the $SiO_2$, and the wavelength of high absorbance broadens for this reason. In this section, all these phenomena are discussed with underlying physics by appropriate Fig. 11–13 separately. Three different wavelengths with three different absorption levels are discussed here for better understanding. They are $\lambda = 415$nm, which has mid-level absorption of 95.6%, $\lambda = 498.25$nm, which has the highest absorption of 99.99%, and $\lambda = 690$nm which has comparatively low absorption compared to the previous two wavelengths, with 91.8% for TE and TM mode for normal incidence.

Figure 11 shows a strong E-field for both TE and TM mode with three different wavelengths mentioned above. This is one of the most important reason for high absorption discussed previously. It is seen that the E-field is highly confined by the dielectric layer $SiO_2$, which enlivens the electric resonance dipolar moment that can be seen in Fig. - 11(d) and (h) for both TE and TM. The electric-field mainly distributed in the center of the structure. The high spots of the E-field are mainly detected on the interfaces of the metal resonator/dielectric layer, which described the increasing surface plasmon effect shown by Fig. 11(a)-(c) and (e)-(f). These surface plasmons created a perfect resonant dipole to magnify the localized E-field [40], [106]. Therefore, increased surface plasmons at the interfaces with the strong optical properties of tungsten guided the MMA for high absorption for those wavelengths.

Magnetic-field exhibited in Fig. 12, for three different wavelengths in TE and TM mode as like as E-field. Like reliable and distributed E-field, the design has a very good distributed H-field, which ushered the structure to a very good polarization-independent MMA for the whole optical region. Fig. 12(a)–(c) and (e)–(g) show that the magnetic field is highly localized on the metal resonator and extensively confined by the dielectric layer, which can be seen from Fig. 12(d) and (h). For the peak absorption level at $\lambda = 498.25$nm, the H-field is very strong for both TE and TM modes as can be seen from Fig. 12(b) and (f), which operates different directions. The cross-sectional view at

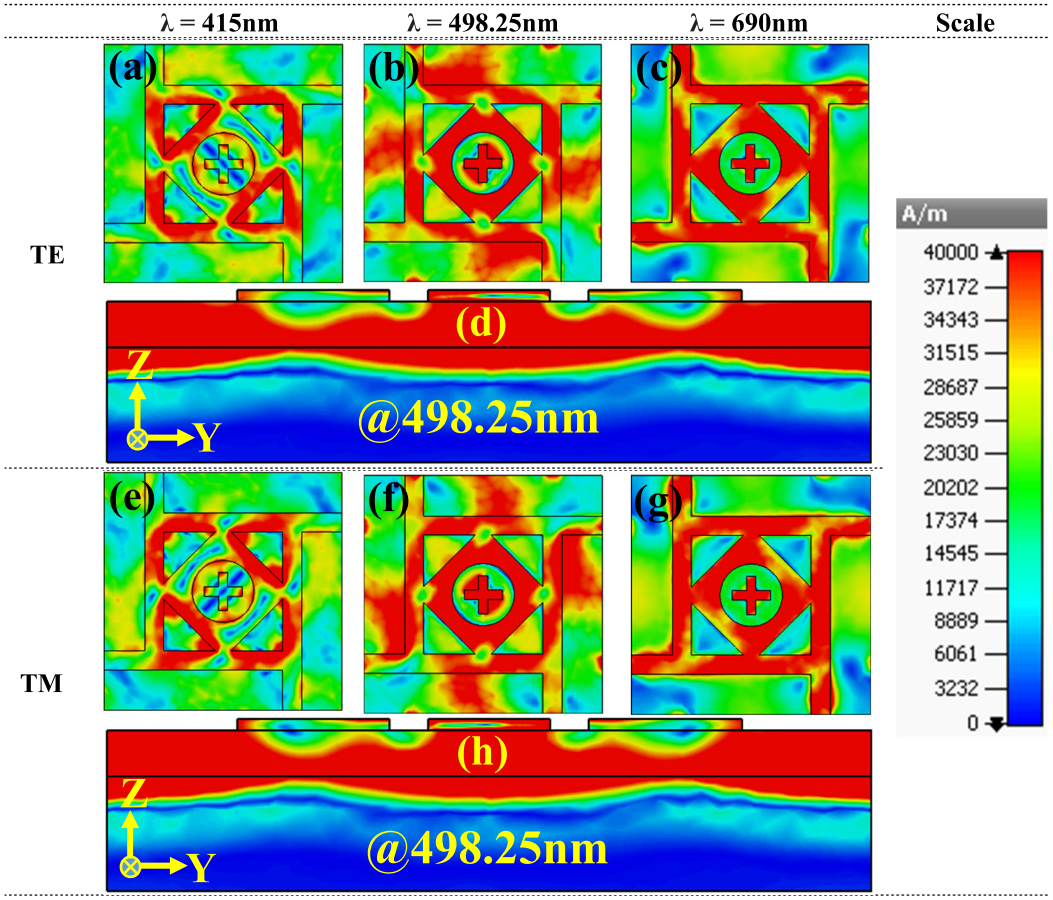


**FIGURE 12.** Representation of magnetic-field distribution of the unit cell (a)-(c) for TE polarization in 415nm, 498.25nm, and 690nm with linear color bar ($Am^{-1}$) in y-x axis, (d) cross-sectional view of the middle of the structure at 498.25 (peak) resonance wavelength in z-y axis, (e)-(g) TM polarization in 415nm, 498.25nm, and 690nm with the same linear color bar ($Am^{-1}$) in y-x axis, (h) cross-sectional view of the middle of the structure at 498.25 (peak) resonance wavelength in z-y axis for normal incidence angle.

$\lambda = 498.25$nm also confirms that the magnetic-field intensity is vigorous in the center of the structure. The H-field only changes its direction as the polarization mode varies from TE to TM. Anti-parallel current density from the metal layer to the metal resonator creates a loop. Artificial magnetic dipolar moment rises by the current density which is interrelated highly with the H-field [41], [107]. Therefore, the structure creates an excitation for the H-field and insinuates a very strong magnetic resonant dipole and creates a very good absorbance for the whole optical region. Another important phenomenon has been confirmed by Figs. 12(d) and (h), that the thickness of the back-layer metal completely blocks the transmission for TE, TM, or TEM mode.

With high E-field and H-field, a good surface charge distribution is another main reason for good absorbance over a wide bandwidth. Fig. 13(a)–(c) and (d)–(f), demonstrate surface charge distribution for the both TE and TM modes respectively. It can be seen from the figure that at $\lambda = 498.25$nm, the surface charge is very widely distributed throughout the whole unit cell. For the TE and TM modes, only the direction of propagation changes. However, for $\lambda = 415$nm and $\lambda = 690$nm, distribution is less than at $\lambda = 498.25$nm. This uniform anti-parallel circulating surface charge distribution is a reason for the high electromagnetic field created in the dielectric layer by the structure discussed above [22], [53], [108].

### J. COMPARATIVE STUDY

As mentioned earlier, an MMA that covers the full optical region is highly desirable. In this section, a comparison of the structure is made with ones in several recent studies with similar features and similar wavelength ranges. From Table 2, it can be seen that in many details this design is superior to other designs published to date. First of all, in this project, the design consisted of an ultrathin with materials of a much higher temperature table than others. As this proposed MMA is supposed to operate in the solar spectrum, high temperature stability is a must. Secondly, the materials used in this structure are more cost-effective than other materials like gold, silicon, and others. Thirdly, a significant feature is that the structure is highly operative

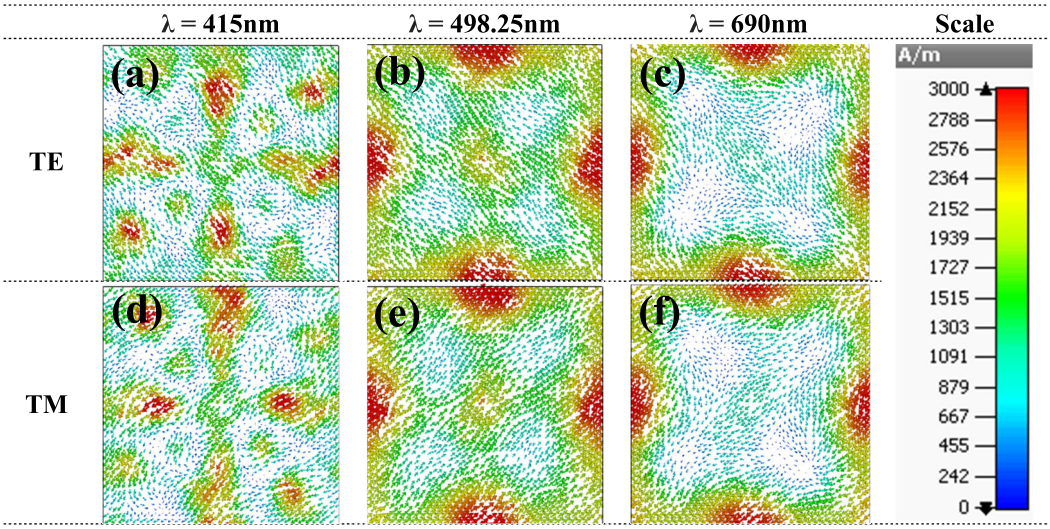


**FIGURE 13.** Representation of cross-sectional view of surface charge distribution of the unit cell (a)-(c) for TE polarization in 415nm, 498.25nm, and 690nm with linear color bar ($Am^{-1}$) in y-x axis, (d)-(f) TM polarization in 415nm, 498.25nm, and 690nm with a linear color bar ($Am^{-1}$) in y-x axis for normal incidence angle. The cross-section is done with an x-y axis.

at an incident angle of up to 60°, which is very important for energy harvesting or sensor applications. Another essential feature is that, as it uses tungsten as the base metal, it does not have to use quartz or a glass layer like other structures have to use. Thus, this feature will reduce the cost of producing this design. With high bandwidth, a high absorption peak of 99.99%, and the features mentioned above, the proposed MMA is a substantial candidate for various optical region applications.

## IV. CONCLUSION

In conclusion, a polarization-insensitive MMA has been designed, simulated, theoretically proved, and optimized for the optical region with an average absorption of 96.7% and a peak of 99.99%. The proposed structure is ultrathin as its thickness is 225nm, using a low refractive index dielectric layer, with a very good impedance match metal tungsten for the optical region with a sandwiched three-layer structure. Also, lossless resonance characteristics of $SiO_2$, incorporated with intrinsic losses of tungsten, enable the design to have excellent absorption. A high electromagnetic field with a distributed surface distribution also perceived by the structure. Also, excellent plasmonic coupling capacitance and inductance between the metal layer and metal resonator leads the design with excellent confinement of the EM wave. Furthermore, the proposed design can be used in UV–OPT–NIR as it has above 90.22% absorption from 300nm to 1000nm. The high melting point of tungsten and silicon dioxide with a wide incident angle makes this design a perfect candidate for solar energy harvesting, STPV, and solar cell applications. A unique feature of linear change of resonant wavelength, makes this design an excellent optical sensor, and a dielectric detector. Changing the dielectric layer to $Si_3N_4$ allows the model used as a light detection sensor or THz light detector. With the large demand of the optical field, the proposed design may be used as a real invisible cloak, thermal detector, light trapper, imaging, magnetic resonance imaging, plasmonic sensor, optical modulator, and other high temperature stable optical wavelength applications.

## REFERENCES

[1] V. G. Veselago, "The electrodynamics of substances with simultaneously negative values of $\varepsilon$ and $\mu$," *Sov. Phys. Uspekhi*, vol. 10, no. 4, p. 509, 1968.

[2] D. R. Smith, W. J. Padilla, D. C. Vier, S. C. Nemat-Nasser, and S. Schultz, "Composite medium with simultaneously negative permeability and permittivity," *Phys. Rev. Lett.*, vol. 84, no. 18, pp. 4184–4187, May 2000, doi: 10.1103/PhysRevLett.84.4184.

[3] M. M. Hasan, M. R. I. Faruque, and M. T. Islam, "Dual band metamaterial antenna for LTE/Bluetooth/WiMAX system," *Sci. Rep.*, vol. 8, no. 1, pp. 1–17, Dec. 2018, doi: 10.1038/s41598-018-19705-3.

[4] F. Fan, X. Zhang, S. Li, D. Deng, N. Wang, H. Zhang, and S. Chang, "Terahertz transmission and sensing properties of microstructured PMMA tube waveguide," *Opt. Express*, vol. 23, no. 21, p. 27204, Oct. 2015, doi: 10.1364/oe.23.027204.

[5] J. Alam, M. R. I. Faruque, and M. T. Islam, "Labyrinth double split open loop resonator based bandpass filter design for S, c and X-band application," *J. Phys. D, Appl. Phys.*, vol. 51, no. 26, Jul. 2018, Art. no. 265102, doi: 10.1088/1361-6463/aac569.

[6] S. Islam, M. Faruque, and M. Islam, "A near zero refractive index metamaterial for electromagnetic invisibility cloaking operation," *Materials*, vol. 8, no. 8, pp. 4790–4804, Jul. 2015, doi: 10.3390/ma8084790.

[7] A. S. Rana, M. Q. Mehmood, H. Jeong, I. Kim, and J. Rho, "Tungsten-based ultrathin absorber for visible regime," *Sci. Rep.*, vol. 8, no. 1, pp. 2–9, Dec. 2018, doi: 10.1038/s41598-018-20748-9.

[8] S. Yin, J. Zhu, W. Xu, W. Jiang, J. Yuan, G. Yin, L. Xie, Y. Ying, and Y. Ma, "High-performance terahertz wave absorbers made of silicon-based metamaterials," *Appl. Phys. Lett.*, vol. 107, no. 7, Aug. 2015, Art. no. 073903, doi: 10.1063/1.4929151.

[9] M. I. Hossain, M. R. I. Faruque, and M. T. Islam, "Analysis on the effect of the distances and inclination angles between human head and mobile phone on SAR," *Prog. Biophys. Mol. Biol.*, vol. 119, no. 2, pp. 103–110, Nov. 2015, doi: 10.1016/j.pbiomolbio.2015.03.008.

[10] M. R. I. Faruque and M. T. Islam, "Design of miniaturized double-negative material for specific absorption rate reduction in human head," *PLoS ONE*, vol. 9, no. 10, Oct. 2014, Art. no. e109947, doi: 10.1371/journal.pone.0109947.

[11] J. Y. Suen, K. Fan, J. Montoya, C. Bingham, V. Stenger, S. Sriram, and W. J. Padilla, "Multifunctional metamaterial pyroelectric infrared detectors," *Optica*, vol. 4, no. 2, p. 276, Feb. 2017, doi: 10.1364/optica.4.000276.

[12] J. A. Montoya, Z.-B. Tian, S. Krishna, and W. J. Padilla, "Ultra-thin infrared metamaterial detector for multicolor imaging applications," *Opt. Express*, vol. 25, no. 19, p. 23343, Sep. 2017, doi: 10.1364/oe.25.023343.

[13] D. Schurig, "An aberration-free lens with zero F-number," in *Proc. Imag. Syst.*, 2010, Art. no. 115034, doi: 10.1364/is.2010.imc1.

[14] X. Zhang and Z. Liu, "Superlenses to overcome the diffraction limit," *Nature Mater.*, vol. 7, no. 6, pp. 435–441, Jun. 2008, doi: 10.1038/nmat2141.

[15] F. Li, H. Chen, Q. He, Y. Zhou, L. Zhang, X. Weng, H. Lu, J. Xie and L. Deng, "Design and implementation of metamaterial polarization converter with the reflection and transmission polarization conversion simultaneously," *J. Opt.*, vol. 21, no. 4, 2019, Art. no. 045102.

[16] G. Duan, J. Schalch, X. Zhao, J. Zhang, R. D. Averitt, and X. Zhang, "An air-spacer terahertz metamaterial perfect absorber for sensing and detection applications," in *Proc. 19th Int. Conf. Solid-State Sensors, Actuat. Microsyst. (TRANSDUCERS)*, Jun. 2017, pp. 1999–2002, doi: 10.1109/TRANSDUCERS.2017.7994463.

[17] L. Xie, W. Gao, J. Shu, Y. Ying, and J. Kono, "Extraordinary sensitivity enhancement by metasurfaces in terahertz detection of antibiotics," *Sci. Rep.*, vol. 5, no. 1, pp. 1–4, Aug. 2015, doi: 10.1038/srep08671.

[18] H. Kim, D. Lee, and S. Lim, "A fluidically tunable metasurface absorber for flexible large-scale wireless ethanol sensor applications," *Sensors*, vol. 16, no. 8, p. 1246, Aug. 2016, doi: 10.3390/s16081246.

[19] A. Salleh, C. C. Yang, T. Alam, M. S. J. Singh, M. Samsuzzaman, and M. T. Islam, "Development of microwave brain stroke imaging system using multiple antipodal vivaldi antennas based on raspberry Pi technology," *J. Kejuruterran*, vol. 32, p. 11, Feb. 2020, doi: 10.17576/jkukm-2020-32(1)-06.

[20] N. I. Landy, S. Sajuyigbe, J. J. Mock, D. R. Smith, and W. J. Padilla, "Perfect metamaterial absorber," *Phys. Rev. Lett.*, vol. 100, no. 20, 2008, Art. no. 207402, doi: 10.1103/PhysRevLett.100.207402.

[21] H. Tao, N. I. Landy, C. M. Bingham, X. Zhang, R. D. Averitt, and W. J. Padilla, "A metamaterial absorber for the terahertz regime: Design, fabrication and characterization," *Opt. Express*, vol. 16, no. 10, p. 7181, May 2008, doi: 10.1364/oe.16.007181.

[22] N. Liu, M. Mesch, T. Weiss, M. Hentschel, and H. Giessen, "Infrared perfect absorber and its application as plasmonic sensor," *Nano Lett.*, vol. 10, no. 7, pp. 2342–2348, Jul. 2010, doi: 10.1021/nl9041033.

[23] Z. H. Jiang, S. Yun, F. Toor, D. H. Werner, and T. S. Mayer, "Conformal dual-band near-perfectly absorbing mid-infrared metamaterial coating," *ACS Nano*, vol. 5, no. 6, pp. 4641–4647, Jun. 2011, doi: 10.1021/nn2004603.

[24] P. Rufangura and C. Sabah, "Dual-band perfect metamaterial absorber for solar cell applications," *Vacuum*, vol. 120, pp. 68–74, Oct. 2015, doi: 10.1016/j.vacuum.2015.05.033.

[25] L. Zhao, H. Liu, Z. He, and S. Dong, "Theoretical design of twelve-band infrared metamaterial perfect absorber by combining the dipole, quadrupole, and octopole plasmon resonance modes of four different ring-strip resonators," *Opt. Express*, vol. 26, no. 10, p. 12838, May 2018, doi: 10.1364/oe.26.012838.

[26] S. Huang, Z. Xie, W. Chen, J. Lei, F. Wang, K. Liu, and L. Li, "Metasurface with multi-sized structure for multi-band coherent perfect absorption," *Opt. Express*, vol. 26, no. 6, p. 7066, Mar. 2018, doi: 10.1364/oe.26.007066.

[27] G. Yao, F. Ling, J. Yue, C. Luo, J. Ji, and J. Yao, "Dual-band tunable perfect metamaterial absorber in the THz range," *Opt. Express*, vol. 24, no. 2, p. 1518, Jan. 2016, doi: 10.1364/oe.24.001518.

[28] H. Li, L. Wang, and X. Zhai, "Tunable graphene-based mid-infrared plasmonic wide-angle narrowband perfect absorber," *Sci. Rep.*, vol. 6, Nov. 2016, Art. no. 36651, doi: 10.1038/srep36651.

[29] Z. Liu, G. Liu, X. Liu, Y. Wang, and G. Fu, "Titanium resonators based ultra-broadband perfect light absorber," *Opt. Mater.*, vol. 83, pp. 118–123, Sep. 2018, doi: 10.1016/j.optmat.2018.06.008.

[30] X. Tian and Z.-Y. Li, "Visible-near infrared ultra-broadband polarization-independent metamaterial perfect absorber involving phase-change materials," *Photon. Res.*, vol. 4, no. 4, p. 146, Aug. 2016, doi: 10.1364/prj.4.000146.

[31] J. Wang, Y. Chen, J. Hao, M. Yan, and M. Qiu, "Shape-dependent absorption characteristics of three-layered metamaterial absorbers at near-infrared," *J. Appl. Phys.*, vol. 109, no. 7, Apr. 2011, Art. no. 074510, doi: 10.1063/1.3573495.

[32] D. Li, H. Huang, H. Xia, J. Zeng, H. Li, and D. Xie, "Temperature-dependent tunable terahertz metamaterial absorber for the application of light modulator," *Results Phys.*, vol. 11, pp. 659–664, Dec. 2018, doi: 10.1016/j.rinp.2018.10.014.

[33] X. Zhang, Y. Fan, L. Qi, and H. Li, "Broadband plasmonic metamaterial absorber with fish-scale structure at visible frequencies," *Opt. Mater. Express*, vol. 6, no. 7, p. 2448, Jul. 2016, doi: 10.1364/ome.6.002448.

[34] N. Mattiucci, M. J. Bloemer, N. Aközbek, and G. D'Aguanno, "Impedance matched thin metamaterials make metals absorbing," *Sci. Rep.*, vol. 3, no. 1, pp. 1–11, Dec. 2013, doi: 10.1038/srep03203.

[35] R. Contractor, G. D'Aguanno, and C. Menyuk, "Ultra-broadband, polarization-independent, wide-angle absorption in impedance-matched metamaterials with anti-reflective moth-eye surfaces," *Opt. Express*, vol. 26, no. 18, p. 24031, Sep. 2018, doi: 10.1364/oe.26.024031.

[36] Y. C. Lai, C. Y. Chen, Y.-T. Hung, and C.-Y. Chen, "Extending absorption edge through the hybrid resonator-based absorber with wideband and near-perfect absorption in visible region," *Materials*, vol. 13, no. 6, p. 1470, 2020, doi: 10.3390/ma13061470.

[37] K. Aydin, V. E. Ferry, R. M. Briggs, and H. A. Atwater, "Broadband polarization-independent resonant light absorption using ultrathin plasmonic super absorbers," *Nature Commun.*, vol. 2, no. 1, pp. 1–7, Sep. 2011, doi: 10.1038/ncomms1528.

[38] T. S. Tuan and N. T. Q. Hoa, "Numerical study of an efficient broadband metamaterial absorber in visible light region," *IEEE Photon. J.*, vol. 11, no. 3, Jun. 2019, Art. no. 4600810, doi: 10.1109/JPHOT.2019.2910806.

[39] D. Katrodiya, C. Jani, V. Sorathiya, and S. K. Patel, "Metasurface based broadband solar absorber," *Opt. Mater.*, vol. 89, pp. 34–41, Mar. 2019, doi: 10.1016/j.optmat.2018.12.057.

[40] X. Han, K. He, Z. He, and Z. Zhang, "Tungsten-based highly selective solar absorber using simple nanodisk array," *Opt. Express*, vol. 25, no. 24, p. A1072, Nov. 2017, doi: 10.1364/oe.25.0a1072.

[41] S. Lee, T. Q. Tran, H. Heo, M. Kim, and S. Kim, "A proposal of a perfect graphene absorber with enhanced design and fabrication tolerance," *Sci. Rep.*, vol. 7, no. 1, pp. 1–10, Dec. 2017, doi: 10.1038/s41598-017-04995-w.

[42] C. Li, H. Fan, Q. Dai, Z. Wei, S. Lan, and H. Liu, "Multipole resonance in arrays of diamond dielectric: A metamaterial perfect absorber in the visible regime," *Nanomaterials*, vol. 9, no. 9, p. 1222, Aug. 2019, doi: 10.3390/nano9091222.

[43] Y. Matsuno and A. Sakurai, "Perfect infrared absorber and emitter based on a large-area metasurface," *Opt. Mater. Express*, vol. 7, no. 2, p. 618, Feb. 2017, doi: 10.1364/ome.7.000618.

[44] X.-J. He, S.-T. Yan, Q.-X. Ma, Q.-F. Zhang, P. Jia, F.-M. Wu, and J.-X. Jiang, "Broadband and polarization-insensitive terahertz absorber based on multilayer metamaterials," *Opt. Commun.*, vol. 340, pp. 44–49, Apr. 2015, doi: 10.1016/j.optcom.2014.11.068.

[45] N. T. Q. Hoa, P. D. Tung, P. H. Lam, N. D. Dung, and N. H. Quang, "Numerical study of an ultrabroadband, wide-angle, polarization-insensitivity metamaterial absorber in the visible region," *J. Electron. Mater.*, vol. 47, no. 5, pp. 2634–2639, May 2018, doi: 10.1007/s11664-018-6100-5.

[46] H. Lin, B. C. P. Sturmberg, K.-T. Lin, Y. Yang, X. Zheng, T. K. Chong, C. M. de Sterke, and B. Jia, "A 90-nm-thick graphene metamaterial for strong and extremely broadband absorption of unpolarized light," *Nature Photon.*, vol. 13, no. 4, pp. 270–276, Apr. 2019, doi: 10.1038/s41566-019-0389-3.

[47] H. Xiong, J.-S. Hong, C.-M. Luo, and L.-L. Zhong, "An ultrathin and broadband metamaterial absorber using multi-layer structures," *J. Appl. Phys.*, vol. 114, no. 6, Aug. 2013, Art. no. 064109, doi: 10.1063/1.4818318.

[48] M. Zhong, "Enhance of the absorption and bandwidth based on a ultra-thin tungsten structure metamaterial absorber in 400–1500 nm range," *Opt. Laser Technol.*, vol. 127, Jul. 2020, Art. no. 106142, doi: 10.1016/j.optlastec.2020.106142.

[49] A. Vora, J. Gwamuri, N. Pala, A. Kulkarni, J. M. Pearce, and D. Ö. Güney, "Exchanging ohmic losses in metamaterial absorbers with useful optical absorption for photovoltaics," *Sci. Rep.*, vol. 4, no. 1, p. 4901, May 2015, doi: 10.1038/srep04901.

[50] X. Zhao, Y. Wang, J. Schalch, G. Duan, K. Cremin, J. Zhang, C. Chen, R. D. Averitt, and X. Zhang, "Optically modulated ultra-broadband all-silicon metamaterial terahertz absorbers," *ACS Photon.*, vol. 6, no. 4, pp. 830–837, Apr. 2019, doi: 10.1021/acsphotonics.8b01644.

[51] Y. P. Lee, P. V. Tuong, H. Y. Zheng, J. Y. Rhee, and W. H. Jang, "An application of metamaterials: Perfect absorbers," *J. Korean Phys. Soc.*, vol. 60, no. 8, pp. 1203–1206, Apr. 2012, doi: 10.3938/jkps.60.1203.

[52] M. J. Hossain, M. R. I. Faruque, M. R. Ahmed, M. J. Alam, and M. T. Islam, "Polarization-insensitive infrared-visible perfect metamaterial absorber and permittivity sensor," *Results Phys.*, vol. 14, Sep. 2019, Art. no. 102429, doi: 10.1016/j.rinp.2019.102429.

[53] M. K. Hedayati, M. Javaherirahim, B. Mozooni, R. Abdelaziz, A. Tavassolizadeh, V. S. K. Chakravadhanula, V. Zaporojtchenko, T. Strunkus, F. Faupel, and M. Elbahri, "Design of a perfect black absorber at visible frequencies using plasmonic metamaterials," *Adv. Mater.*, vol. 23, no. 45, pp. 5410–5414, Dec. 2011, doi: 10.1002/adma.201102646.

[54] W. Li, U. Guler, N. Kinsey, G. V. Naik, A. Boltasseva, J. Guan, V. M. Shalaev, and A. V. Kildishev, "Refractory plasmonics with titanium nitride: Broadband metamaterial absorber," *Adv. Mater.*, vol. 26, no. 47, pp. 7959–7965, Dec. 2014, doi: 10.1002/adma.201401874.

[55] T. Cao, C.-W. Wei, R. E. Simpson, L. Zhang, and M. J. Cryan, "Broadband polarization-independent perfect absorber using a phase-change metamaterial at visible frequencies," *Sci. Rep.*, vol. 4, no. 1, p. 3955, May 2015, doi: 10.1038/srep03955.

[56] S. Cao, W. Yu, T. Wang, Z. Xu, C. Wang, Y. Fu, and Y. Liu, "Two-dimensional subwavelength meta-nanopillar array for efficient visible light absorption," *Appl. Phys. Lett.*, vol. 102, no. 16, 2013, Art. no. 161109, doi: 10.1063/1.4803046.

[57] W. Zhu, F. Xiao, I. D. Rukhlenko, J. Geng, X. Liang, M. Premaratne, and R. Jin, "Wideband visible-light absorption in an ultrathin silicon nanostructure," *Opt. Express*, vol. 25, no. 5, p. 5781, Mar. 2017, doi: 10.1364/oe.25.005781.

[58] Z. Liu, X. Liu, S. Huang, P. Pan, J. Chen, G. Liu, and G. Gu, "Automatically acquired broadband plasmonic-metamaterial black absorber during the metallic film-formation," *ACS Appl. Mater. Interfaces*, vol. 7, no. 8, pp. 4962–4968, Mar. 2015, doi: 10.1021/acsami.5b00056.

[59] M. Luo, S. Shen, L. Zhou, S. Wu, Y. Zhou, and L. Chen, "Broadband, wide-angle, and polarization-independent metamaterial absorber for the visible regime," *Opt. Express*, vol. 25, no. 14, pp. 16715–16724, 2017, doi: 10.1364/OE.25.016715.

[60] M. H. Heidari and S. H. Sedighy, "Broadband wide-angle polarization-insensitive metasurface solar absorber," *J. Opt. Soc. Amer. A, Opt. Image Sci.*, vol. 35, no. 4, p. 522, Apr. 2018, doi: 10.1364/josaa.35.000522.

[61] X. Duan, S. Chen, W. Liu, H. Cheng, Z. Li, and J. Tian, "Polarization-insensitive and wide-angle broadband nearly perfect absorber by tunable planar metamaterials in the visible regime," *J. Opt.*, vol. 16, no. 12, Dec. 2014, Art. no. 125107, doi: 10.1088/2040-8978/16/12/125107.

[62] M. Desouky, A. M. Mahmoud, and M. A. Swillam, "Silicon based mid-IR super absorber using hyperbolic metamaterial," *Sci. Rep.*, vol. 8, no. 1, pp. 8–15, Dec. 2018, doi: 10.1038/s41598-017-18737-5.

[63] R. Maas, H. Schokker, J. Parsons, and A. Polman, "Experimetal realization of a polarization-independent ultraviolet/visible coaxial plasmonic metamaterial," *Nano Lett.*, vol. 14, no. 11, pp. 6356–6360, 2013, doi: 10.1021/nl5028183.

[64] H.-E. Su, J.-L. Li, and L. Xia, "A novel temperature controlled broadband metamaterial absorber for THz applications," *IEEE Access*, vol. 7, pp. 161255–161263, 2019, doi: 10.1109/ACCESS.2019.2950729.

[65] N. Mishra, D. K. Choudhary, R. Chowdhury, K. Kumari, and R. K. Chaudhary, "An investigation on compact ultra-thin triple band polarization independent metamaterial absorber for microwave frequency applications," *IEEE Access*, vol. 5, pp. 4370–4376, 2017, doi: 10.1109/ACCESS.2017.2675439.

[66] W. Zuo, Y. Yang, X. He, D. Zhan, and Q. Zhang, "A miniaturized metamaterial absorber for ultrahigh-frequency RFID system," *IEEE Antennas Wireless Propag. Lett.*, vol. 16, pp. 329–332, 2017, doi: 10.1109/LAWP.2016.2574885.

[67] L. Zigoneanu, B.-I. Popa, A. F. Starr, and S. A. Cummer, "Design and measurements of a broadband two-dimensional acoustic metamaterial with anisotropic effective mass density," *J. Appl. Phys.*, vol. 109, no. 5, Mar. 2011, Art. no. 054906, doi: 10.1063/1.3552990.

[68] C. Shao, H. Long, Y. Cheng, and X. Liu, "Low-frequency perfect sound absorption achieved by a modulus-near-zero metamaterial," *Sci. Rep.*, vol. 9, no. 1, p. 13482, Dec. 2019, doi: 10.1038/s41598-019-49982-5.

[69] C. Wu, B. Neuner, III, J. John, A. Milder, B. Zollars, S. Savoy, and G. Shvets, "Metamaterial-based integrated plasmonic absorber/emitter for solar thermo-photovoltaic systems," *J. Opt.*, vol. 14, no. 2, Feb. 2012, Art. no. 024005, doi: 10.1088/2040-8978/14/2/024005.

[70] C. Liang, Y. Zhang, Z. Yi, X. Chen, Z. Zhou, H. Yang, Y. Yi, Y. Tang, W. Yao, and Y. Yi, "A broadband and polarization-independent metamaterial perfect absorber with monolayer Cr and Ti elliptical disks array," *Results Phys.*, vol. 15, Dec. 2019, Art. no. 102635, doi: 10.1016/j.rinp.2019.102635.

[71] A. Xomalis, I. Demirtzioglou, Y. Jung, E. Plum, C. Lacava, P. Petropoulos, D. J. Richardson, and N. I. Zheludev, "Cryptography in coherent optical information networks using dissipative metamaterial gates," *APL Photon.*, vol. 4, no. 4, Apr. 2019, Art. no. 046102, doi: 10.1063/1.5092216.

[72] H. A. bruckl Shoshi, W. Reichi, G. Niessner, and T. Maier, "Wavelength-selective metamaterial absorber for thermal detectors," in *Proc. AMA Conf.*, 2015, pp. 251–256, doi: 10.5162/sensor2015/B4.1.

[73] Y. Tang, S. Ren, H. Meng, F. Xin, L. Huang, T. Chen, C. Zhang, and T. J. Lu, "Hybrid acoustic metamaterial as super absorber for broadband low-frequency sound," *Sci. Rep.*, vol. 7, no. 1, p. 43340, Mar. 2017, doi: 10.1038/srep43340.

[74] K. Shi, G. Jin, R. Liu, T. Ye, and Y. Xue, "Underwater sound absorption performance of acoustic metamaterials with multilayered locally resonant scatterers," *Results Phys.*, vol. 12, pp. 132–142, Mar. 2019, doi: 10.1016/j.rinp.2018.11.060.

[75] P. V. Tuong, J. W. Park, V. D. Lam, W. H. Jang, S. A. Nikitov, and Y. P. Lee, "Dielectric and ohmic losses in perfectly absorbing-metamaterials," *Opt. Commun.*, vol. 295, pp. 17–20, May 2013, doi: 10.1016/j.optcom.2013.01.031.

[76] N. I. Landy, C. M. Bingham, T. Tyler, N. Jokerst, D. R. Smith, and W. J. Padilla, "Design, theory, and measurement of a polarization-insensitive absorber for terahertz imaging," *Phys. Rev. B, Condens. Matter*, vol. 79, no. 12, Mar. 2009, Art. no. 125104, doi: 10.1103/PhysRevB.79.125104.

[77] Y. Gong, Z. Li, J. Fu, Y. Chen, G. Wang, H. Lu, L. Wang, and X. Liu, "Highly flexible all-optical metamaterial absorption switching assisted by kerr-nonlinear effect," *Opt. Express*, vol. 19, no. 11, p. 10193, May 2011, doi: 10.1364/oe.19.010193.

[78] P. Wu, C. Zhang, Y. Tang, B. Liu, and L. Lv, "A perfect absorber based on similar fabry-perot four-band in the visible range," *Nanomaterials*, vol. 10, no. 3, p. 488, 2020, doi: 10.3390/nano10030488.

[79] H. Ma, K. Song, L. Zhou, and X. Zhao, "A naked eye refractive index sensor with a visible multiple peak metamaterial absorber," *Sensors*, vol. 15, no. 4, pp. 7454–7461, Mar. 2015, doi: 10.3390/s150407454.

[80] P. Moitra, B. A. Slovick, W. Li, I. I. Kravchencko, D. P. Briggs, S. Krishnamurthy, and J. Valentine, "Large-scale all-dielectric metamaterial perfect reflectors," *ACS Photon.*, vol. 2, no. 6, pp. 692–698, Jun. 2015, doi: 10.1021/acsphotonics.5b00148.

[81] K. Du, Q. Li, W. Zhang, Y. Yang, and M. Qiu, "Wavelength and thermal distribution selectable microbolometers based on metamaterial absorbers," *IEEE Photon. J.*, vol. 7, no. 3, Jun. 2015, Art. no. 6800908, doi: 10.1109/JPHOT.2015.2406763.

[82] T. Alam, M. Faruque, and M. Islam, "A double-negative metamaterial-inspired mobile wireless antenna for electromagnetic absorption reduction," *Materials*, vol. 8, no. 8, pp. 4817–4828, Jul. 2015, doi: 10.3390/ma8084817.

[83] H. Lin, X. Ye, X. Chen, Z. Zhou, Z. Yi, G. Niu, Y. Yi, Y. Hua, J. Hua, and S. Xiao, "Plasmonic absorption enhancement in graphene circular and elliptical disk arrays," *Mater. Res. Express*, vol. 6, no. 4, p. 45807, 2019, doi: 10.1088/2053-1591/aafc3e.

[84] W. Li and J. Valentine, "Metamaterial perfect absorber based hot electron photodetection," *Nano Lett.*, vol. 14, no. 6, pp. 3510–3514, Jun. 2014, doi: 10.1021/nl501090w.

[85] M. Bağmanci, M. Karaaslan, E. Ünal, O. Akgol, and C. Sabah, "Extremely-broad band metamaterial absorber for solar energy harvesting based on star shaped resonator," *Opt. Quantum Electron.*, vol. 49, no. 7, pp. 1–14, Jul. 2017, doi: 10.1007/s11082-017-1091-7.
[86] B. Mulla and C. Sabah, "Multiband metamaterial absorber design based on plasmonic resonances for solar energy harvesting," *Plasmonics*, vol. 11, no. 5, pp. 1313–1321, Oct. 2016, doi: 10.1007/s11468-015-0177-y.
[87] R. Schmidt and A. Webb, "Metamaterial combining electric-and magnetic-dipole-based configurations for unique dual-band signal enhancement in ultrahigh-field magnetic resonance imaging," *ACS Appl. Mater. Interfaces*, vol. 9, no. 40, pp. 34618–34624, 2017, doi: 10.1021/acsami.7b06949.
[88] J. Grant, M. Kenney, Y. D. Shah, I. Escorcia-Carranza, and D. R. S. Cumming, "CMOS compatible metamaterial absorbers for hyperspectral medium wave infrared imaging and sensing applications," *Opt. Express*, vol. 26, no. 8, p. 10408, Apr. 2018, doi: 10.1364/oe.26.010408.
[89] M. T. Islam, A. Hoque, A. F. Almutairi, and N. Amin, "Left-handed metamaterial-inspired unit cell for S-Band glucose sensing application," *Sensors*, vol. 19, no. 1, p. 169, 2019, doi: 10.3390/s19010169.
[90] Z. Yi, J. Chen, C. Cen, X. Chen, Z. Zhou, Y. Tang, X. Ye, S. Xiao, W. Luo, and P. Wu, "Tunable graphene-based plasmonic perfect metamaterial absorber in the THz region," *Micromachines*, vol. 10, no. 3, p. 194, Mar. 2019, doi: 10.3390/mi10030194.
[91] K. V. Sreekanth, M. ElKabbash, R. Medwal, J. Zhang, T. Letsou, G. Strangi, M. Hinczewski, R. S. Rawat, C. Guo, and R. Singh, "Generalized brewster angle effect in thin-film optical absorbers and its application for graphene hydrogen sensing," *ACS Photon.*, vol. 6, no. 7, pp. 1610–1617, Jul. 2019, doi: 10.1021/acsphotonics.9b00564.
[92] G. Ghosh, "Dispersion-equation coefficients for the refractive index and birefringence of calcite and quartz crystals," *Opt. Commun.*, vol. 163, nos. 1–3, pp. 95–102, 1999, doi: 10.1016/S0030-4018(99)00091-7.
[93] Philip M, Schneider, and W. B. Fowler, "Band structure and optical properties of silicon dioxide," *Phys. Rev. Lett.*, vol. 36, no. 8, p. 425, 1976.
[94] M. Esposito, V. Tasco, F. Todisco, M. Cuscunà, A. Benedetti, M. Scuderi, G. Nicotra, and A. Passaseo, "Programmable extreme chirality in the visible by helix-shaped metamaterial platform," *Nano Lett.*, vol. 16, no. 9, pp. 5823–5828, Sep. 2016, doi: 10.1021/acs.nanolett.6b02583.
[95] Y. Cui, K. H. Fung, J. Xu, H. Ma, Y. Jin, S. He, and N. X. Fang, "Ultrabroadband light absorption by a sawtooth anisotropic metamaterial slab," *Nano Lett.*, vol. 12, no. 3, pp. 1443–1447, Mar. 2012, doi: 10.1021/nl204118h.
[96] J. Zhou, A. F. Kaplan, L. Chen, and L. J. Guo, "Experiment and theory of the broadband absorption by a tapered hyperbolic metamaterial array," *ACS Photon.*, vol. 1, no. 7, pp. 618–624, Jul. 2014, doi: 10.1021/ph5001007.
[97] T. T. Nguyen and S. Lim, "Wide incidence angle-insensitive metamaterial absorber for both TE and TM polarization using eight-circular-sector," *Sci. Rep.*, vol. 7, no. 1, p. 3204, Dec. 2017, doi: 10.1038/s41598-017-03591-2.
[98] Y. Qi, Y. Zhang, C. Liu, T. Zhang, B. Zhang, and L. Wang, "A tunable terahertz metamaterial absorber composed of hourglass-shaped graphene arrays," *Nanomaterials*, vol. 10, no. 3, p. 533, 2020, doi: 10.3390/nano10030533.
[99] Z. Mao, S. Liu, B. Bian, B. Wang, and B. Ma, "Multi-band polarization-insensitive metamaterial absorber based on Chinese ancient coin-shaped structures," *J. Appl. Phys.*, vol. 115, May 2014, Art. no. 204505, doi: 10.1063/1.4878697.
[100] Y. Qi, C. Liu, B. Hu, X. Deng, and X. Wang, "Tunable plasmonic absorber in THz-band range based on graphene 'arrow' shaped metamaterial," *Results Phys.*, vol. 15, Dec. 2019, Art. no. 102777, doi: 10.1016/j.rinp.2019.102777.
[101] E. J. Rothwell, J. L. Frasch, S. M. Ellison, P. Chahal, and R. O. Ouedraogo, "Analysis of the nicolson-ross-weir method for characterizing the electromagnetic properties of engineered materials," *Prog. Electromagn. Res.*, vol. 157, pp. 31–47, 2016, doi: 10.2528/PIER16071706.
[102] T. Wanghuang, W. Chen, Y. Huang, and G. Wen, "Analysis of metamaterial absorber in normal and oblique incidence by using interference theory," *AIP Adv.*, vol. 3, no. 10, Oct. 2013, Art. no. 102118, doi: 10.1063/1.4826522.
[103] H.-T. Chen, "Interference theory of metamaterial perfect absorbers," *Opt. Express*, vol. 20, no. 7, p. 7165, Mar. 2012, doi: 10.1364/oe.20.007165.
[104] H.-T. Chen, J. Zhou, J. F. O'Hara, F. Chen, A. K. Azad, and A. J. Taylor, "Antireflection coating using metamaterials and identification of its mechanism," *Phys. Rev. Lett.*, vol. 105, no. 7, Aug. 2010, Art. no. 073901, doi: 10.1103/PhysRevLett.105.073901.
[105] D. R. Smith, D. C. Vier, T. Koschny, and C. M. Soukoulis, "Electromagnetic parameter retrieval from inhomogeneous metamaterials," *Phys. Rev. E, Stat. Phys. Plasmas Fluids Relat. Interdiscip. Top.*, vol. 71, no. 3, Mar. 2005, Art. no. 036617, doi: 10.1103/PhysRevE.71.036617.
[106] H. M. Lee and J. C. Wu, "A wide-angle dual-band infrared perfect absorber based on metal–dielectric–metal split square-ring and square array," *J. Phys. D, Appl. Phys.*, vol. 45, no. 20, 2012, Art. no. 205101, doi: 10.1088/0022-3727/45/20/205101.
[107] T. Cao, L. Zhang, R. E. Simpson, and M. J. Cryan, "Mid-infrared tunable polarization-independent perfect absorber using a phase-change metamaterial," *J. Opt. Soc. Amer. B, Opt. Phys.*, vol. 30, no. 6, p. 1580, Jun. 2013, doi: 10.1364/josab.30.001580.
[108] N. Liu, H. Guo, L. Fu, S. Kaiser, H. Schweizer, and H. Giessen, "Three-dimensional photonic metamaterials at optical frequencies," *Nature Mater.*, vol. 7, no. 1, pp. 31–37, Jan. 2008, doi: 10.1038/nmat2072.
[109] H. Xu, L. Hu, Y. Lu, J. Xu, and Y. Chen, "Dual-band metamaterial absorbers in the visible and near-infrared regions," *J. Phys. Chem. C*, vol. 123, no. 15, pp. 10028–10033, Apr. 2019, doi: 10.1021/acs.jpcc.9b00434.
[110] M. K. Hedayati, A. U. Zillohu, T. Strunskus, F. Faupel, and M. Elbahri, "Plasmonic tunable metamaterial absorber as ultraviolet protection film," *Appl. Phys. Lett.*, vol. 104, no. 4, 2014, Art. no. 041103, doi: 10.1063/1.4863202.
[111] H. Zhang, C. Guan, J. Luo, Y. Yuan, N. Song, Y. Zhang, J. Fang, and H. Liu, "Facile film-nanoctahedron assembly route to plasmonic metamaterial absorbers at visible frequencies," *ACS Appl. Mater. Interfaces*, vol. 11, no. 22, pp. 20241–20248, Jun. 2019, doi: 10.1021/acsami.9b01088.

**SULTAN MAHMUD** received the B.Sc. degree from the Department of Electrical and Electronic Engineering, International Islamic University Chittagong (IIUC), Bangladesh, in 2020. He is a metamaterial enthusiast. He completed his undergraduate thesis on metamaterial based absorber for optical wavelength applications. His main research interest includes metamaterials and metamaterial absorber for optical applications.

**SIKDER SUNBEAM ISLAM** (Member, IEEE) received the B.Sc. degree in electrical and electronic engineering from Bangladesh, in 2005, the M.Sc. degree in mobile computing and communications from the University of Greenwich, U.K., in 2008, and the Ph.D. degree in space science from the National University of Malaysia, Malaysia, in 2017.

He is currently serving as an Associate Professor and the Department Head with the Department of Electrical and Electronic Engineering, International Islamic University Chittagong, Bangladesh. He has one published book and many publications in international proceedings and journals. His main research interests include metamaterial for communications, electromagnetic radiation, and mobile computing. He has been serving as a reviewer for several international conferences and journals.

**ALI F. ALMUTAIRI** (Senior Member, IEEE) received the B.S. degree in electrical engineering from the University of South Florida, Tampa, Florida, in 1993, and the M.S. and Ph.D. degrees in electrical engineering from the University of Florida, Gainesville, Florida, in 1995 and 2000, respectively.

He served as the Vice Dean for Academic Affairs at the College of Engineering and Petroleum, Kuwait University, from February 2016 to July 2018. He served as the Chairman of the Electrical Engineering Department, Kuwait University, from March 2007 to September 2011, and served as the Graduate Program Director of the Electrical Engineering Department, Kuwait University, from September 2015 to September 2016. He is currently an Associate Professor with the Electrical Engineering Department, Kuwait University, and the Dean of Admission and Registration. His current research interests include multiuser detection, cross-layer design, antenna design, and current and future cellular networks.

Dr. Almutairi is a member of other professional societies. In December 1993, he has been awarded a full scholarship from Kuwait University to pursue his graduate studies. He served/serving as associate editor and a reviewer for many technical publications.

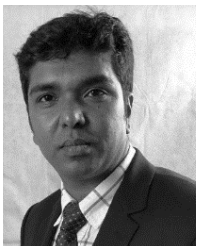

**MOHAMMAD TARIQUL ISLAM** (Senior Member, IEEE) is currently a Professor with the Department of Electrical, Electronic and Systems Engineering, Universiti Kebangsaan Malaysia (UKM), and a Visiting Professor with the Kyushu Institute of Technology, Japan. He is the author or coauthor of about 500 research journal articles, nearly 175 conference articles, and a few book chapters on various topics related to antennas, microwaves, and electromagnetic radiation analysis with 20 inventory patents filed. Thus far, his publications have been cited 6000 times and his H-index is 38 (Source: Scopus). His Google scholar citation is 8200 and H-index is 42. His research interests include communication antenna design, satellite antennas, and electromagnetic radiation analysis.

Dr. Islam was a recipient of more than 40 research grants from the Malaysian Ministry of Science, Technology and Innovation, Ministry of Education, UKM research grant, international research grants from Japan and Saudi Arabia. He received several International Gold Medal awards, a Best Invention in Telecommunication Award for his research and innovation, and Best Researcher Awards, in 2010 and 2011 at UKM. He was a recipient of the 2018 IEEE AP/MTT/EMC Excellent Award. He also won the best innovation award, in 2011, and the Best Research Group in ICT niche, in 2014, by UKM. He was a recipient of Publication Award from Malaysian Space Agency, in 2014, 2013, 2010, and 2009 and the Best Paper Presentation Award, in 2012, International Symposium on Antennas and Propagation, (ISAP 2012) at Nagoya, Japan, and in 2015, in IconSpace. He has supervised about 30 Ph.D. theses, 20 M.Sc. theses, and has mentored more than ten postdocs and Visiting scholars. He is a Chartered Professional Engineer-C.Eng., a member of IET, U.K., and a Senior Member of IEICE, Japan. He currently serves as the Guest Editor of *Sensors* Journal, an Associate Editor of IEEE Access, and he was an Associate Editor of *IET Electronics Letter*.